Reduced Auger recombination in single CdSe/CdS nanorods by one-dimensional electron delocalization

Freddy T. Rabouw,[†] Per Lunnemann,[‡,¶] Relinde J. A. van Dijk-Moes,[†] Martin Frimmer,[‡,§] Francesca Pietra,[†] A. Femius Koenderink,[‡] and Daniël Vanmaekelbergh[*,†]

Condensed Matter and Interfaces, Debye Institute for Nanomaterials Science, Princetonplein 1, 3584 CC Utrecht, The Netherlands, and Center for Nanophotonics, FOM Institute AMOLF, Science Park 104, 1098 XG Amsterdam, The Netherlands

E-mail: d.vanmaekelbergh@uu.nl

[*]To whom correspondence should be addressed

[†]Condensed Matter and Interfaces, Debye Institute for Nanomaterials Science, Princetonplein 1, 3584 CC Utrecht, The Netherlands

[‡]Center for Nanophotonics, FOM Institute AMOLF, Science Park 104, 1098 XG Amsterdam, The Netherlands

[¶]Current address: DTU Fotonik, Department of Photonics Engineering, Technical University of Denmark, DK-2800 Kongens Lyngby, Denmark

[§]Current address: Photonics Laboratory, ETH Zürich, 8093 Zürich, Switzerland

Abstract

Progress to reduce non-radiative Auger decay in colloidal nanocrystals has recently been made by growing thick shells. However, the physics of Auger suppression is not yet fully understood. Here, we examine the dynamics and spectral characteristics of single CdSe-dot-in-CdS-rod nanocrystals. These exhibit blinking due to charging/discharging, as well as trap-related blinking. We show that one-dimensional electron delocalization into the rod-shaped shell can be as effective as a thick spherical shell at reducing Auger recombination of the negative trion state.

Keywords: nanocrystal, colloidal quantum dot, nanorod, blinking, trion, Auger recombination

Random switching, or 'blinking', between bright and dark states is a phenomenon generally observed in fluorescent colloidal nanocrystal quantum dots (QDs) when examined at the single-emitter level.[1,2] The presence of dark states drastically reduces the efficiency of colloidal QDs for example in LEDs, lasers, and solar cells, in bio-imaging, or as reliable single-photon sources. Blinking is commonly understood in terms of the charging/discharging model.[3] According to this model a dark period is initiated if one charge carrier of a photo-excited exciton is trapped at the QD surface or ejected into the surrounding matrix. The remaining carrier quenches photoemission of subsequent excitons by opening a non-radiative Auger recombination pathway, in which it accepts the exciton recombination energy. Many recent experimental findings have been explained in terms of the charging/discharging model.[4–12] However, there are experimental results that pose a challenge to this model.[13–15] Galland *et al.* have proposed that in addition to charging/discharging, there may be a second blinking mechanism related to surface traps.[16]

Recently, a potential solution to the problem of blinking was presented with the introduction of colloidal QDs of CdSe with a thick CdS shell.[4,17] In this system lower-intensity periods are no longer completely dark, but still have approximately 20–30% brightness compared to high-intensity periods. The unusual brightness of lower-intensity periods has been ascribed to suppression of non-radiative Auger recombination in the trion (charged exciton) state. In addition, relatively high biexciton quantum efficiencies[18,19] have been found in these core/shell QDs, also ascribed to slow Auger rates. However, the physical origin of Auger suppression has not yet been clearly identified,[20] mainly because in thick-shell QDs several potentially important properties are combined: a smooth carrier confinement potential due to core/shell interface alloying,[21–23] electron delocalization into the CdS shell, and increased spatial separation between the emitting core and the nanocrystal surface.[12] The latter property combined with a temperature-dependent band offset has been invoked[12] to explain the observation of slow Auger rates at cryogenic temperatures.[6,12,24,25] Moreover, different authors do not even agree on the sign of the charge of the unusually bright trion state.[5–7,10,11,16,25] Clearly, blinking and Auger suppression are not yet entirely understood.

Here, we investigate single CdSe/CdS dot-in-rod structures, nanorods (NRs) of CdS with a

spherical CdSe core. These NRs are presently of high interest due to the easy synthesis procedure, and their high brightness and photostability. Moreover, they have recently been identified as promising single-photon emitters,[26] which can exhibit efficient negative trion emission.[27] They have a peculiar shape and band structure, such that holes are tightly confined to the core, while electrons can delocalize along the long direction of the CdS rod.[28–36] We show that partial electron delocalization in the long direction of the CdS rod can be as effective as the more "conventional" thick spherical CdS shell[4,17] for the suppression of Auger decay.

We perform detailed studies on single NRs using a combination of photoluminescence (PL) decay and time-resolved spectral measurements under ambient conditions. We quantify the rate constants and binding energies of the different states of the NRs. From a comparison of the experimental results with quantum-mechanical effective-mass calculations, we specifically identify lower-intensity periods with the negative trion state, in accordance with Tenne *et al.*[27] Remarkably, we find that our NRs are comparable to the thick-shell (10–12 monolayers) QDs in terms of quantum efficiency of the trion state, although the CdSe core is only covered by a very thin shell of CdS (3 monolayers) in the short direction of the NR. We conclude that electron delocalization in just one dimension (i.e. along the length of the NR) is sufficient to achieve efficient suppression of non-radiative Auger recombination. More precisely, we measure an average Auger lifetime of $11\ \mathrm{ns}$ over 18 single NRs, which is an order of magnitude longer than the lifetime of the negative trion state in spherical thin-shell CdSe/CdS QDs.[37] Our observations illustrate that Auger losses in colloidal nanocrystals can effectively be reduced by wavefunction engineering in specifically designed hetero-structures.

This Letter is organized as follows: first we describe in detail how we quantify the dynamics and transition energies of the states involved in the blinking of a single NR. Using simple effective-mass calculations we then identify that each NR shows blinking between a neutral exciton and a negative trion state. Next, we briefly discuss the two types of blinking statistics observed among the different NRs (exponential and power-law), which indicate that in some NRs there is trap-related blinking in addition to exciton-trion blinking. Finally, we explain the relatively high quantum

efficiency of the negative trion state arguing that Auger recombination is suppressed by the smooth Coulomb potential that binds the partially delocalized electron to the core-confined hole.

Characterization of bright and grey states

We investigate single colloidal NRs with a CdSe dot core of 3.2 nm diameter, and a CdS rod shell of 5.6 nm diameter and 21 nm length (with 10% size polydispersity; see also Fig. 4a). The characterization of a single NR consists of two parts (see Methods for technical details). First, we do time-correlated single-photon counting (TCSPC) for 200 s in a Hanbury Brown-Twiss setup, allowing for the simultaneous acquisition of an intensity trace over time scales of seconds to minutes, the photon-photon correlation function $g^{(2)}$, and PL decay curves. We divide the total measurement time into time bins of 10 ms. For each time bin we extract the number of photon counts, and the PL lifetime by fitting a single-exponential decay function to the histogram (165 ps binning) of delay times between pump pulse and arrival of a fluorescence photon, using a maximum-likelihood routine.[38] Subsequently, we flip a mirror in the detection arm of our setup and record a series of 2000 emission spectra each with an integration time of 20 ms. We fit each 20 ms emission frame to a single Gaussian and extract (1) the integrated emission intensity, and (2) the peak emission wavelength.

We have examined a total of 18 single NRs. Figure 1a shows the results of TCSPC measurements on one of them: the intensity and extracted PL lifetime traces, and the corresponding histograms. The vanishing photon-photon correlation at zero time delay (inset) proves that we are examining a single emitter, and that biexciton emission does not obscure our measurements[39] (see Supplementary Discussion 1 for details). We see that the NR exhibits both intensity blinking and PL lifetime blinking, i.e. random switching between well-defined values for these parameters. Nevertheless, the emission intensity never approaches the background value of 0.1 cts$/10$ ms so the NR always remains emissive. Furthermore, the blinking behavior does not change over the measurement time of 200 s, hence the NR does not degrade. In the intensity histogram (Fig. 1a, top right) we distinguish three states: a bright state with mean emission intensities of $M_{\mathrm{A}} = 179$ cts$/10$ ms

that we label 'A', and two lower-intensity 'grey' states ($M_{\mathrm{B}} = 63\,\mathrm{cts}/10\,\mathrm{ms}$, $M_{\mathrm{C}} = 41\,\mathrm{cts}/10\,\mathrm{ms}$) that we label 'B' and 'C'. The good correspondence to a Poissonian intensity distribution (red line) for each of the three peaks in the histogram indicates that three well-defined states are involved. In order to examine the correlation between intensity and PL lifetime we combine the two traces and obtain the fluorescence-lifetime-intensity-distribution (FLID)[40] of the NR, as presented in Figure 1b. The logarithmic color scale quantifies the frequency of occurrence for a combination of emission intensity and PL lifetime. We notice from the FLID that the bright state A has a long PL lifetime, while the two distinct grey states B and C have shorter PL lifetimes.

Continuing, we focus on the spectral measurements performed on the *same* NR and at the same laser power. Figure 1c shows the integrated intensity and emission wavelength traces, and the corresponding histograms. Still, no degradation of the NR occurs. Intensity and emission wavelength blinking are clearly visible. Again, three peaks appear in the intensity histogram (Fig. 1c, top right). These peaks have the same relative mean intensities and weights (obtained from a fit to three Gaussians; red line) as those in the intensity histogram constructed from the TCSPC data (Fig. 1a). Clearly, in the spectral measurements we resolve and identify the same three states A, B, and C as in the TCSPC measurements. Combination of the intensity and emission wavelength traces yields the emission-wavelength-intensity-distribution (EWID; Figure 1d). We see that the emission wavelengths of states B and C are very close. In fact, state B and C are indistinguishable based on the wavelength histogram *alone* (Fig. 1c) due to fit uncertainties and the fact that each of the states may exhibit spectral diffusion[41,42] comparable to the separation between B and C. Still, the EWID (Fig. 1d) unambiguously shows the presence of two distinct states B and C, that differ slightly in terms of emission wavelength.

In the following we aim to identify the different states from their PL decay and spectral characteristics. Therefore, we assign each time bin from the TCSPC series (Fig. 1a) and each spectral frame from the spectral series (Fig. 1c) to state A, B, or C, based on the clear definition of the three states in the FLID (Fig. 1b) and EWID (Fig. 1d). We obtain the state-averaged PL decay curves and emission spectra, as presented in Figure 2. PL decay curves (Fig. 2a) are excellently fitted

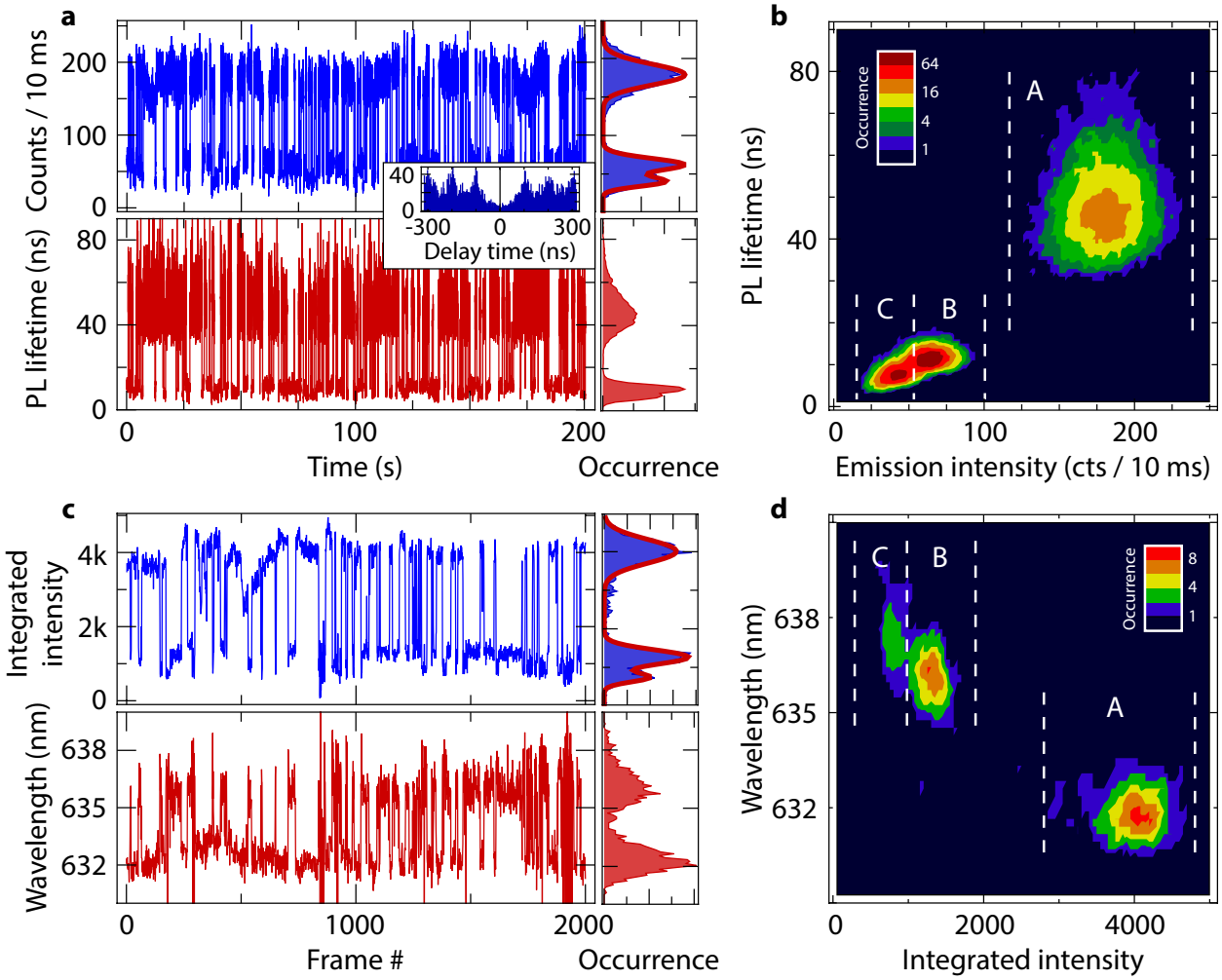

Figure 1: **a)** The intensity trace (top) and PL lifetime trace (bottom) of a single CdSe/CdS NR measured over 200 s using TCSPC, and corresponding histograms (right). We used a time binning of 10 ms. The background counts are less than 0.1 cts/10 ms. Inset: the absence of a zero-delay peak in the photon-photon correlation proves that we are looking at a single NR. **b)** The fluorescence-lifetime-intensity-distribution (FLID) constructed from the data in **a**, indicating in logarithmic color scale the frequency of occurrence for a combination of emission intensity and PL lifetime. The three distinct states A, B, and C are highlighted by dashed lines. **c)** The intensity trace (top) and emission wavelength trace (bottom) of the same single NR measured on the spectrometer, and corresponding histograms (right). Each spectral frame is obtained by integration over 20 ms. **d)** The emission-wavelength-intensity-distribution (EWID) constructed from the data in **c**, indicating in color scale the frequency of occurrence for a combination of integrated intensity and emission wavelength. Again, states A, B, and C are highlighted by dashed lines.

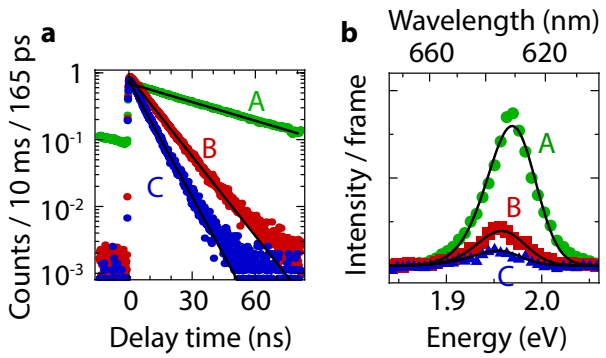

Figure 2: **a)** PL decay curves (semi-log scale) of the states A (green), B (red), and C (blue). Solid black lines are single exponential fits. **b)** Emission spectra of the states A (green circles), B (red squares), and C (blue triangles). Solid lines are fits to a series of phonon replicas with a fixed spacing of $26\ \mathrm{meV}$. See the Methods section for details of the fitting procedure.

with a single-exponential decay. The spectra (Fig. 2b) are asymmetrically broadened towards the low-energy side, and are fitted to a series of phonon replicas with a fixed spacing of $26\ \mathrm{meV}$ (see the Methods section for details). Table 1 summarizes the best-fit values for PL lifetime, PL decay amplitude, and emission wavelength (i.e. zero-phonon peak energy E_0), as well as the photon count rates obtained from the fit to the intensity histogram (Fig. 1a; see above).

Next, we wish to determine the quantum efficiency, η, of the grey states, and quantify the competition between radiative and non-radiative recombination that leads to the unusually high brightness. To this end, we use our fit results from Table 1, and inspired by previous works[7,10] we employ two different methods to estimate radiative and non-radiative contributions to the total decay. In both methods one assumes that the quantum efficiency of the bright state $\eta_{\mathrm{A}} = 1$[7,43–45] (we have measured it to be at least 87%[46]) and that the excitation rate of the emitter is the same in each state (see Supplementary Discussion 2 for comments). In the first method[7] one retrieves the quantum efficiency of grey state i from the photon count rate M: $\eta_i/\eta_{\mathrm{A}} = M_i/M_{\mathrm{A}}$. In the second method[10] one obtains the radiative decay rate $\tau_{\mathrm{r},i}^{-1}$ of state i from the PL decay amplitude: $\tau_{\mathrm{r},i}^{-1}/\tau_{\mathrm{r,A}}^{-1} = A_i/A_{\mathrm{A}}$. Table 1 shows the estimates of quantum efficiency, and radiative and non-radiative decay rates, obtained using the two different methods. Strikingly, the quantum efficiencies of the grey states (B and C) for this NR are very high, even comparable to those encountered in thick-shell CdSe/CdS QDs.[7,9]

Table 1: Characteristics of the three distinct states A, B, and C. Fit results were obtained from fits to the experimental TCSPC and spectral data. Estimates of quantum efficiency, radiative and non-radiative lifetimes are made using two methods, which are described in the text and specified in parentheses in the first column. Error margins represent 95% confidence intervals as obtained from the fitting errors. Additional uncertainty of a few percent stems from the choice of thresholds for the assignment of time slices to a state. For the parameter estimates, origins of error are discussed in the Supplementary Discussion 2. * = by assumption.

		State A	State B	State C
Fit results				
Photon count rate M (cts/10 ms)		179.5 ± 0.9	62.6 ± 0.8	40.8 ± 0.9
PL lifetime τ (ns)		46.4 ± 0.3	11.19 ± 0.08	7.04 ± 0.07
PL decay amplitude A (cts/10 ms/165 ps)		0.632 ± 0.003	0.939 ± 0.009	0.730 ± 0.010
Emission energy E_0 (meV)		1974 ± 3	1961 ± 5	1960 ± 11
Parameter estimates				
Quantum efficiency	(1)	100^*	34.9 ± 0.5	22.7 ± 0.5
η (%)	(2)	100^*	35.9 ± 0.5	17.5 ± 0.3
Radiative lifetime	(1)	46.4 ± 0.3	32.1 ± 0.5	31.0 ± 0.8
τ_{r} (ns)	(2)	46.4 ± 0.3	31.2 ± 0.4	40.1 ± 0.6
Non-rad. lifetime	(1)	∞	17.19 ± 0.23	9.11 ± 0.13
τ_{nr} (ns)	(2)	∞	17.45 ± 0.23	8.54 ± 0.11
Assignment				
		X^0	X^-	

To test whether the results are reproducible we examined 17 more single NRs. The Supplementary Data present a full overview of the characteristics of each of the 18 NRs. All NRs exhibit a clear grey state B similar to the NR discussed in detail above. The characteristics of the lowest-intensity state, however, are much less uniform. Four NRs do not show a third state at all, but only two states A and B. In the other NRs, the lowest-intensity states can be divided into two groups: five NRs have one bright (A) and two grey states (B and C) as encountered for the NR discussed above (Fig. 1). On the other hand, nine NRs show a bright (A) and a grey (B) state in addition to a lowest-intensity state which is almost dark (< 3 cts/10 ms). First, we will focus on characterization and identification of the omnipresent grey state B. Later, we tentatively assign the different lowest-intensity states observed.

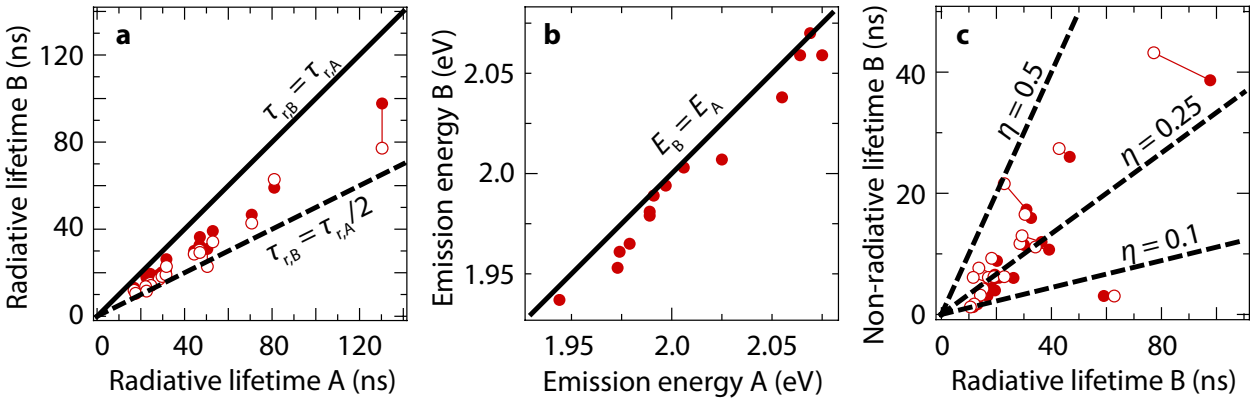

Figure 3: Overview of the characteristics of the bright state A and grey state B for 18 single NRs. Estimates obtained by method 1 (via the photon count rate; see text for details) are given in open circles, those obtained by method 2 (via the PL decay amplitude; see text for details) in closed disks. Solid lines connect symbols that belong to the same NR, i.e. the results of method 1 and 2. Error margins are typically $< 1\%$ (see Table 1) and within the size of the symbols. **a)** The correlation between the radiative lifetimes of the bright state A (the neutral exciton X^0) and the grey state B (the negative trion X^-). Radiative decay is faster in the grey state than in the bright state by a factor $1.51(\pm 0.21)$ (mean $\pm$ standard deviation). **b)** The correlation between the emission energies of the bright and the grey state. Emission from the grey state is lower in energy by $10(\pm 7)$ meV. **c)** The correlation between the radiative and non-radiative lifetimes of the grey state. The resulting quantum efficiency of the grey state is $25(\pm 10)\%$.

Figure 3 summarizes the characteristics of grey state B of the 18 single NRs examined. Figure 3a presents the correlation between the radiative lifetimes of states A and B, estimated using method 1 (via the photon count rate; open circles), and method 2 (via the PL decay amplitude; closed disks). We see that the radiative lifetime is shorter in the grey state B than in the bright state A by a factor of $1.51(\pm 0.21)$ (mean $\pm$ standard deviation). Figure 3b shows the emission energies of states A and B. We see that the emission of the grey state B is consistently lower in energy than the emission of the bright state A, by $10(\pm 7)$ meV. In Figure 3c we plot the radiative and non-radiative lifetimes of state B [indicating the two methods for parameter estimation with open circles (method 1) and closed disks (method 2), as in Fig. 3a]. We see that in all NRs the radiative decay of state B is competitive with non-radiative decay, resulting in quantum efficiencies as high as $25(\pm 10)\%$. Figure S1 shows that the trends observed in Fig. 3 are robust to more conservative estimates of $\eta_{\mathrm{A}} = 0.75$ and a 20% lower excitation rate of state B compared to state A, rather than $\eta_{\mathrm{A}} = 1$ and equal excitation rates.

The increased radiative decay rate of the grey state compared to the bright state (Fig. 3a) is a strong indication in favor of the charging/discharging model. Radiative decay rates increase with the number of charge carriers in the system.[10,16] Alternative models, which invoke the presence of trap-related non-radiative decay channels during low-intensity periods,[47,48] cannot account for an increase in radiative decay rate. Hence, we conclude that bright periods (state A) correspond to the neutral state of the emitter, where emission originates from the uncharged exciton X^0. During grey periods (state B) the emitter is charged, and emission originates from a trion, i.e. a charged exciton.

The effect of electron delocalization

In previous studies there has even been disagreement on the sign of the trion charge associated with the observed grey states.[5,7,10,11,16] Here, by comparison of the experimental results to quantum-mechanical effective-mass calculations we will show that the grey state B in our NRs is the negative trion state. To this end, we calculate radiative decay rates and transition energies of the neutral exciton X^0, negative trion X^-, and positive trion X^+. Details of the calculation method can be found in the Supplementary Methods. Briefly, we model the NR as the three-dimensional system depicted in Figure 4a [the actual NRs examined (Fig. 4b) exhibit 10% size polydispersity]. The CdSe core is assumed to act as an infinite potential well for the hole.[49] The electron, on the other hand, is free to find the optimal extent of (de)localization under the influence of Coulomb attraction of the hole, a small conduction band (CB) offset, the different effective masses in CdS and CdSe, and (for the case of the two electrons in X^-) Coulomb repulsion of the other electron.

Figures 4c,d present the results of our effective-mass calculations: the transition energies (c) and the radiative lifetimes (d) of the neutral exciton X^0, the negative trion X^- and the positive trion X^+. On the x-axis we varied the CB offset between $0\ \mathrm{meV}$[50] and $300\ \mathrm{meV}$[51] (with the CdSe core having the lower CB minimum), since its value is not well established in literature and is assumed to depend for example on strain in the nanocrystal.[52] The sensitivity of the CB offset may also partially explain the wide spread in radiative lifetimes that we find in our system experimentally,

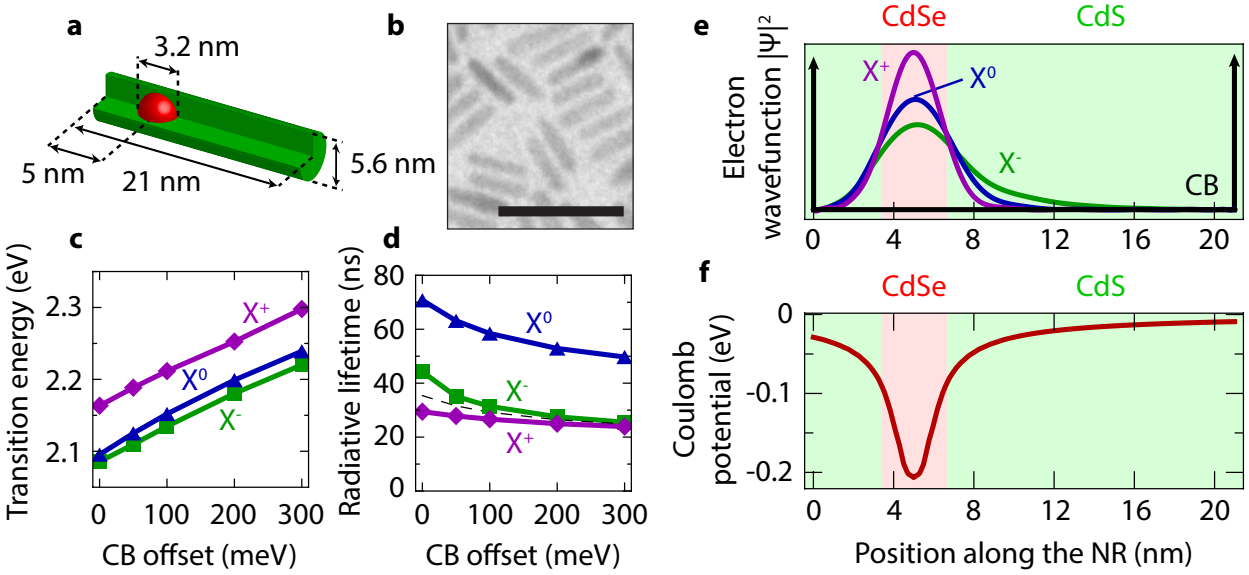

Figure 4: **a)** The dimensions of the model NR used for the effective-mass calculation. The spherical CdSe core of 3.2 nm diameter is embedded in a cylindrical CdS rod of 5.6 nm diameter and 21 nm length, and positioned with its centre at 5 nm from one end of the rod. **b)** A transmission electron micrograph of the nanorods. Scale bar is 40 nm. **c)** The transition energy and **d)** radiative lifetime of X^-, X^0 and X^+, calculated for different values of CB offset. The dashed line in **(d)** represents radiative decay which is exactly twice faster than in X^0. **e)** The normalized electron wavefunctions $|\Psi|^2$ in the different states, showing the variable extent of electron localization (calculated for a CB offset of 0 meV). The thick black line represents the CB potential experienced by the electron (not including Coulomb interactions), with the small CB offset between CdSe and CdS and an infinite potential outside the NR. **f)** The soft potential well experienced by the electron due to electron-hole Coulomb attraction. See the Supplementary Methods for details of the calculation method.

and has been found for single thick-shell CdSe/CdS QDs.[10] The calculated binding energies of X^- and X^+ are consistent with previous assignments of emission spectra of ensembles of charged QDs,[53,54] as well as single QDs at cryogenic temperatures.[6,24] The experimental transition energy difference between state B and state A is $10\ \mathrm{meV}$ (Fig. 3b), in close agreement with the calculated 10-19 meV difference (Fig 4c; depending on the value of the CB offset) between X^- and X^0 [see also Supplementary Discussion 3]. Furthermore, the experimental ratio of radiative lifetimes $\tau_{\mathrm{r,A}}/\tau_{\mathrm{r,B}}$ is 1.51 (Fig. 3a), in fair agreement with the calculated ratio of $\tau_{\mathrm{r},X^0}/\tau_{\mathrm{r},X^-} = 1.60$–$1.95$ (Fig. 4d). For the positive trion X^+, on the other hand, the calculations predict characteristics that are totally inconsistent with grey state B: approximately 60 meV *higher* transition energy, and a shorter radiative lifetime by a factor 2.1–2.4 compared to X^0. Accordingly, we identify the bright state A and the grey state B as the neutral exciton X^0 and the negative trion X^-, respectively.

Remarkably, we find, experimentally and theoretically, that the negative trion has a slower radiative decay rate than predicted by statistical scaling relations which are often used for rate estimates.[10,11,37] Scaling of the radiative rate with the number of recombination pathways would lead to a radiative rate of X^- that is twice faster than for X^0, since the hole has twice as many electrons with which to recombine.[10] However, the electron-hole overlap integrals in X^- and X^0 are different. Figure 4d shows the electron wavefunctions in the X^+, X^0 and X^- states calculated for a CB offset of $0\ \mathrm{meV}$. Clearly, the extent of electron localization varies significantly between the states. More precisely, electron-electron Coulomb repulsion enhances delocalization in X^- compared to X^0. Due to a smaller electron-hole overlap integral, radiative recombination via either pathway in X^- is slower than in X^0. As a result, the radiative decay for X^- is faster by a factor smaller than two (see Fig. 4d). Indeed, we have measured that $\tau_{\mathrm{r,A}}/\tau_{\mathrm{r,B}} = 1.51$, which is 25% off the value of $\tau_{\mathrm{r},X^0}/\tau_{\mathrm{r},X^-} = 2$ that one would expect from statistical scaling.[10] The 25% deviation is a direct manifestation of electron delocalization.

Analysis of the lowest-intensity states

Next, we focus on the lowest-intensity states, which are intrinsically hard to characterize due to the low signal. We can divide the 18 NRs examined (Supplementary Data) into two groups. Group 1 (containing NRs #1, 2, 4, 5, 6, 7, 10, 17, 18) shows only bright $\leftrightarrow$ grey blinking, i.e. the brightness does not fall below 20% of the brightest state. In five of these (NRs #4, 5, 6, 10, 17) there are two distinct grey states B and C (Figure 1), while the other four appear to have only one grey state B. Group 2, on the other hand, contains NRs (the other nine) showing bright $\leftrightarrow$ grey blinking in addition to a "'dark state" with emission intensity $< 3\ \mathrm{cts}/10\ \mathrm{ms}$. This dark state, that we label "D", is very different from the grey states B and C as we will show below. Figure 5a presents the intensity histograms of two NRs, representative for group 1 (left) and group 2 (right). We have labeled the different states A, B, C and D according to their emission intensities. We clearly see that only the NR on the right exhibits a dark state D with $< 3\ \mathrm{cts}/10\ \mathrm{ms}$. Figure 5b shows the blinking statistics of these two NRs (left and right). We plot the bright/dim duration probability distributions,[55,56] using the threshold intensities indicated by the dashed lines in Fig. 5a. The two NRs have qualitatively different duration probability distributions, which are representative for the other NRs of the respective groups. NRs *without* a dark state (group 1; Fig. 5 left) show exponential distributions, while those *with* a dark state (group 2; Fig. 5 right) show power-law distributions. Based on the bright/dim statistics, and on the PL decay and spectral properties, we will now make assignments, first for the grey state C (Fig. 5a left) and then for the dark state D (Fig. 5a right).

The characteristics of grey state C (Table 1) differ only slightly from the X^- state B: roughly 30% lower emission intensity, 30% shorter PL lifetime, and equal emission energy. Furthermore, the exponential statistics associated with a state C (Fig. 5 left) indicates that A $\leftrightarrow$ C blinking involves an Auger-assisted charging mechanism following the occasional creation of a biexciton and with a well-defined rate constant.[57] In fact, exponential statistics have been found for $X^0 \leftrightarrow X^-$ blinking in thick-shell CdSe/CdS QDs.[10,16] We propose that grey state C is a negative trion X^- that differs from the X^- state B by *the location where the ejected hole resides*.[40] Indeed, the charging/discharging model for blinking involves ejection of a charge (here, the hole) that

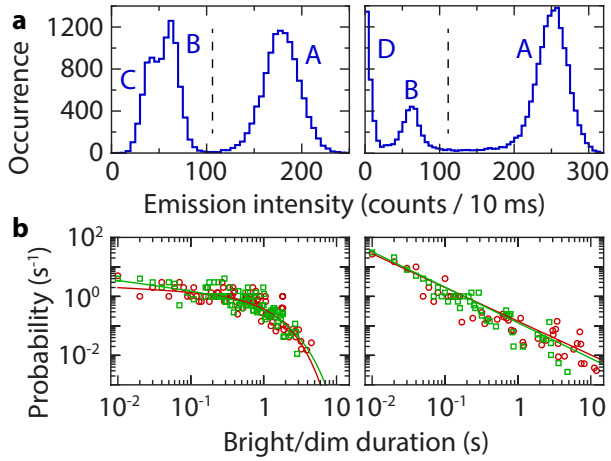

Figure 5: **a)** Intensity histograms of a NR from the first group (with a grey state C; left) and of a NR from the second group (with a dark state D; right). Binning: 5 counts. **b)** The corresponding probability duration distributions of the bright periods (state A; red circles), and dim periods (states B + C/D; green squares) for the NR from group 1 (left), and the NR from group 2 (right). The intensity thresholds used are depicted by dashed lines in **a**.

resides on the surface or in the environment of the NR for some time before returning. Due to the anisotropic shape of the NRs, there may be two possible types of locations for the ejected hole to reside, giving rise to two negative trion states X^- with similar but slightly different characteristics.

We can model the effect of the ejected hole by a single positive point charge on the NR surface in our effective-mass model. We put a point charge at the tip or at the side (nearest to the core) of the NR, 1 nm from the surface. We can then compare the resulting transition energy and radiative lifetime of the X^- state to the above calculations in which we neglected the ejected hole. Using a conduction band offset of -100 meV the changes are -3 meV and -1.6 ns for the charge at the tip, and -5 meV and -1.6 ns for the charge at the side. Hence, the ejected hole may indeed be responsible for the small distinction between the B and C states. However, the effects are so small that we cannot make statements about exactly where the ejected hole resides in the experiment.

The different statistics (Fig. 5b) imply that two completely different mechanisms underlie A $\leftrightarrow$ D blinking and A $\leftrightarrow$ B,C blinking. Moreover, state D (NRs from group 2; Fig. 5 right) has very different properties from states B and C: very low emission intensity ($< 3\%$ compared to the X^0 state) and very short PL lifetime (1–2 ns). In addition, PL decay curves of state D have a lower amplitude (see Supplementary Data) than those of the X^0 state. This indicates that state

D is, in fact, not a charged state, since an extra charge would lead to an increased radiative rate and with that a *higher* PL decay amplitude for state D (see above). Hence, we tentatively assign blinking to state D to the opening and closing of trap states. The trap model has been used before to explain the power-law statistics encountered in many single emitters (but which we find exclusively in NRs with a state D), including conventional QDs.[2,55,56] Our results seem to comfirm those of Galland *et al.*[16] and Tenne *et al.*[27] who found that blinking can be due to *combination* of charging/discharging and opening/closing of trap states, but that the two blinking mechanisms are distinct in terms of the blinking statistics. Note, however, that our state D has a short PL lifetime (indicating that traps capture charge carriers from the lowest energy exciton) whereas in Ref.[16] the PL lifetime of the trap-related low-intensity state has a long PL lifetime (indicating that traps only capture hot charge carriers that have not yet relaxed to the band edge). Ref.[27] does not investigate the PL dynamics of the trap-related state.

Suppression of Auger recombination

We now return to the main focus of this paper which is the properties of the negatively charged state B. We recognize the non-radiative lifetimes of state B (Fig. 3c) as Auger lifetimes of X^-. Auger recombination is slow enough that radiative decay can compete with it, resulting in X^- quantum efficiencies in our NRs (25%) as high as those observed in thick-shell CdSe/CdS QDs with 12 monolayer ($5\ \mathrm{nm}$) thick shells.[7,9] This finding is consistent with the recent observations of reduced blinking[26] and efficient negative trion emission[27] in CdSe/CdS NRs. However, it is remarkable if we consider that in our system the CdSe core is covered by a cylindrical CdS shell that is only 3 monolayers thin in the direction perpendicular to the long NR axis. The average Auger lifetime of $11\ \mathrm{ns}$ (distributed from $1.2\ \mathrm{ns}$ to $40.9\ \mathrm{ns}$) is still an order of magnitude longer than observed in *spherical* thin-shell (2–3 monolayers) CdSe/CdS QDs.[37] Apparently, merely one-dimensional electron delocalization results in efficient Auger suppression in the negative trion state.

Our NRs are different from thick-shell QDs in terms of two important properties that have previously been argued to be responsible for a suppression of Auger recombination. First, the NRs

have only a small separation between the emitting core and the outer surface. Apparently, charge carriers reaching the outer surface of a nanocrystal do not necessarily lead to efficient Auger decay. This finding seems to contrast with the model of Javaux *et al.*[12] who attribute the suppression of Auger recombination in core/shell QDs at cryogenic temperatures to surface assisted Auger decay combined with temperature-dependent band offsets. Second, (unintentional) interfacial alloying[8,22,23] is most likely absent in our NRs, as evidenced by the low biexciton quantum efficiency (see Fig. 1a) and the short reaction time during synthesis (a few minutes[29] versus many hours for the thick-shell QDs[17]). We conclude that interfacial alloying is also no strict requirement to achieve suppression of Auger decay. We must, however, point out that we cannot exclude other subtle differences between our NRs and thick-shell QDs in terms of strain fields[52,58–60] or stacking faults.[61] More in-depth experimental[62] and theoretical work will have to be performed to quantify these differences and their potential effect on charge carrier dynamics.

We can qualitatively explain the occurrence of suppressed Auger decay in our NRs in terms of the simple theoretical model of Cragg and Efros.[21] They argued that the Auger recombination rate roughly scales with high spatial-frequency components of the charge carrier wavefunctions, and that those high-frequency components are reduced in amplitude if the confinement potential experienced by the excess carrier is smoothened or 'softened'.[21,63] Based on this argumentation, Auger suppression has been linked to soft confinement potentials due to core/shell interface alloying.[8,22,23] Interestingly, in our NRs the confinement potential experienced by the electron is also soft, but for another reason. The extent of electron localization is namely dictated by long-range Coulomb attraction of the hole, which is tightly confined to the core. The softness of the Coulomb confinement potential is evident from Fig. 4f. Soft confinement leads to partial electron delocalization that allows for substantial radiative recombination (which does require electron-hole overlap), while restraining high-frequency components in the electron wavefunction (limiting Auger decay). As a consequence, in our NRs the negative trion has a high quantum efficiency. In fact, Auger suppression in thick-shell CdSe/CdS QDs may also in large part be enabled by the softness of the electron-hole Coulomb attraction. Indeed, also in the thick-shell systems the extent of electron

delocalization is set by the Coulomb potential of the core-confined hole. However, this effect has so far mostly been overlooked in favor of the interface alloying model.[21]

Our findings point towards a new design rule for nanocrystals with reduced Auger recombination. As an alternative method to core/shell interface alloying,[8,22,23] a soft confinement potential can also result from electron delocalization and long-range electron-hole Coulomb interaction (Fig. 4f). Generalizing, we suggest that Auger recombination in nanostructures may be suppressed if the extent of confinement of the excess carrier is mainly set by Coulomb attraction of opposite charges rather than spatial confinement (as in conventional or thin-shell QDs). Indeed, relatively slow biexciton Auger decay has recently been found in spherical "type-II" InP/CdS QDs,[64] where Coulomb interaction is an important factor determining the shape of charge carrier wavefunctions. Moreover, Auger decay is slow in bulk semiconductors,[65,66] where Coulomb interaction is the only interaction that binds electron-hole pairs.

We must emphasize that while our NRs are an excellent model system to study the effect of delocalization on Auger recombination, only Auger decay of the negative trion X^- is suppressed. Auger decay of excitonic states with an excess hole [biexcitons X_2 and possibly positive trions X^+] is still efficient (see also Supplementary Discussion 1), because holes experience hard confinement by the large CdSe/CdS valence band offset. New nanostructure designs, aimed at increasing the importance of Coulomb interactions for the extent of confinement of both electrons and holes, may lead to suppression of Auger losses for all excitonic states. Wavefunction engineering promises to be a good strategy to achieve this goal, facilitated by the tremendous progress made in recent years in controlling the shape and composition of colloidal hetero-systems.[67] As an example, in Figure S2 we propose a colloidal nanostructure in which both electrons and holes can partially delocalize, and which promises to have suppressed Auger recombination in all excitonic states but efficient radiative recombination due to the presence of direct electron-hole overlap. To summarize, we have identified the negative trion state in blinking CdSe/CdS NRs based on its PL decay and spectral characteristics (i.e. faster radiative decay by a factor 1.51 and a lower transition energy by $10\ \mathrm{meV}$ compared to the neutral exciton). These characteristics are a direct consequence of the

shape and band alignment of our hetero-structure. Furthermore, we have explained the blinking behavior involving multiple states as encountered in many of the NRs. Most importantly, we have quantified the suppression of non-radiative Auger recombination in the negative trion state, which leads to the quantum efficiency as high as 25%. Strikingly, this value is comparable to those reported for thick-shell CdSe/CdS QDs.[7,9] We attribute Auger suppression to the fact that the extension of the electron wavefunction is mainly dictated by a soft Coulomb confinement potential. We envision that our work will lead to new strategies for the minimization of non-radiative Auger losses that currently form a major obstacle for the application of colloidal nanocrystals in devices.

Methods

The NRs examined in this study were synthesized following the method of Carbone *et al.*,[29] and then coated with a thin layer of silica following Ref.[68] The NRs have an ensemble quantum yield of 74%, measured using an integrating sphere. The silica layer serves as protection against photo bleaching.[69] Furthermore, we found that silica coated NRs cluster less than bare ones. We deposited the NRs on a glass slide from a dilute dispersion in ethanol. We used the microscope setup depicted and described in Ref.[70] All measurements were performed in ambient conditions. Single NRs were excited with $10\ \mathrm{ps}$, $10\ \mathrm{MHz}$, $532\ \mathrm{nm}$ linearly polarized pulses generated by a frequency doubled Nd:YVO_4 laser, through an oil immersion objective with a magnification of 100 and numerical aperture (NA) 1.4. We used a laser power of $200\ \mathrm{nW}$ focused to a diffraction-limited spot. From the count rate of the high-intensity state of single NRs (approximately 20 kHz), the estimated collection efficiency of our microscope setup (10%) and detection efficiency of our detectors (10%), we estimate that at this laser intensity we create $\langle N \rangle \approx 0.2$ excitons per laser pulse. This corresponds well to the value of $\langle N \rangle \approx 0.1$ excitons estimated from the absorption cross-section of the NRs ($\sigma_{\mathrm{abs}} \approx 10^{-15}\ \mathrm{cm}^2$ at $532\ \mathrm{nm}$).[30,71] Fluorescence light was collected through the same objective used for excitation, and separated from laser reflections using a long-pass filter with a cut-off at $590\ \mathrm{nm}$. For timing and photon-photon correlation measurements we used a Hanbury Brown-Twiss setup with two ID Quantique id100-20 ULN avalanche photo-diodes (APDs;

dark counts < 10 Hz) connected to a timing card (DPC 230, Becker & Hickl GmbH) with 165 ps time resolution. Spectral measurements were done with an Acton Research SpectraPro 2300i spectrograph equipped with a PIXIS:100B back-illuminated Si CCD array by Princeton Instruments. We remark that the CCD camera used for spectral measurements required a few ms read-out time between successive frames. We used single exponential decay functions to fit the state-resolved PL decay curves (Fig. 2a and panels c of the Supplementary Data):

$$I(t) = A \exp\left(-t/\tau\right), \tag{1}$$

where the fit parameters A and τ are the PL decay amplitude and PL lifetime, respectively. We used a maximum-likelihood routine for the fits,[38] assuming Poissonian statistics. A flat background was not included since the dark count rate of our detectors is < 10 cts/s. For PL decay curves with a longer lifetime tail, we fitted only to the single exponential early-time signal. The values of the PL decay amplitudes A given (Table 1 and the summarizing tables in the Supplementary Data) are corrected for the relatively short laser repetition period ($T = 100$ ns) of our setup compared to the PL lifetimes (τ = 5–50 ns): $A \rightarrow A/[1 + \exp\left(-T/\tau\right)]$. A correction is needed because the tail of a PL decay curve with $t > T$ is counted towards the early-time signal ($t \rightarrow t - T$), as clearly visible in the PL decay curve of state A (Fig. 2a and panels c in the Supplementary Data): the signal at negative delay is the tail of the PL decay that extends over longer than 100 ns.

State-averaged emission spectra (Fig. 2b and panels e in the Supplementary Data) are asymmetrically broadened towards the red side due to exciton-phonon coupling. They were fitted to a series of phonon replicas at fixed energy intervals of $\epsilon_{\mathrm{LO}} = 26$ meV (the longitudinal optical phonon energy in CdSe) using a nonlinear least-squares method:

$$I(E) = I_0 \sum_{n=0}^{5} \frac{S^n}{n!} \exp\left[-\frac{1}{2}\left(\frac{E - E_0 + n\epsilon_{\mathrm{LO}}}{\sigma}\right)^2\right], \tag{2}$$

Here the fit parameters I_0, E_0, σ and S are the peak amplitude, zero-phonon peak energy, peak width and Huang-Rhys factor, respectively. We obtained typical values for the Huang-Rhys factor

of S = 0.3–1.2. The choice for a Gaussian lineshape for each phonon replica is set by broadening due to coupling to lower-energy phonon modes. We find typical values for the peak width of σ = 30–40 meV.

Acknowledgement

This work is part of the research program of the "Stichting voor Fundamenteel Onderzoek der Materie (FOM)", which is financially supported by the "Nederlandse Organisatie voor Wetenschappelijk Onderzoek (NWO)". PL gratefully acknowledges the Carlsberg Foundation for financial support. AFK gratefully acknowledges an NWO-Vidi grant for financial support.

Supporting Information Available

Supplementary data of all the single NRs examined; a description of the effective-mass model used; a discussion of the methods used to estimate rate constants, including the assumptions made; the proposal of a ternary nanocrystal that should have reduced Auger recombination in all excitatonic states; a discussion of the biexciton quantum efficiency; a discussion of the transition energies. This material is available free of charge via the Internet at `http://pubs.acs.org/`.

References

(1) Nirmal, M.; Dabbousi, B. O.; Bawendi, M. G.; Macklin, J. J.; Trautman, J. K.; Harris, T. D.; Brus, L. E. *Nature* **1996**, *383*, 802–804.

(2) Frantsuzov, P.; Kuno, M.; Jankó, B.; Marcus, R. A. *Nature Phys.* **2008**, *4*, 519–522.

(3) Efros, A.; Rosen, M. *Phys. Rev. Lett.* **1997**, *78*, 1110–1113.

(4) Mahler, B.; Spinicelli, P.; Buil, S.; Quelin, X.; Hermier, J.-P.; Dubertret, B. *Nature Mater.* **2008**, *7*, 659–664.

(5) Gómez, D. E.; Van Embden, J.; Mulvaney, P.; Fernée, M. J.; Rubinsztein-Dunlop, H. *ACS Nano* **2009**, *3*, 2281–2287.

(6) Fernée, M. J.; Littleton, B. N.; Rubinsztein-Dunlop, H. *ACS Nano* **2009**, *3*, 3762–3768.

(7) Spinicelli, P.; Buil, S.; Quélin, X.; Mahler, B.; Dubertret, B.; Hermier, J.-P. *Phys. Rev. Lett.* **2009**, *102*, 136801.

(8) Wang, X.; Ren, X.; Kahen, K.; Hahn, M. A.; Rajeswaran, M.; Maccagnano-Zacher, S.; Silcox, J.; Cragg, G. E.; Efros, A. L.; Krauss, T. D. *Nature* **2009**, *459*, 686–689.

(9) Malko, A. V.; Park, Y.-S.; Sampat, S.; Galland, C.; Vela, J.; Chen, Y.; Hollingsworth, J. A.; Klimov, V. I.; Htoon, H. *Nano Lett.* **2011**, *11*, 5213–5218.

(10) Galland, C.; Ghosh, Y.; Steinbrück, A.; Hollingsworth, J. A.; Htoon, H.; Klimov, V. I. *Nat. Commun.* **2012**, *3*, 908.

(11) Qin, W.; Shah, R. A.; Guyot-Sionnest, P. *ACS Nano* **2012**, *6*, 912–918.

(12) Javaux, C.; Mahler, B.; Dubertret, B.; Shabaev, A.; Rodina, A. V.; Efros, A. L.; Yakovlev, D. R.; Liu, F.; Bayer, M.; Camps, G.; Biadala, L.; Buil, S.; Quelin, X.; Hermier, J.-P. *Nature Nanotech.* **2013**, *8*, 206–212.

(13) Zhao, J.; Nair, G.; Fisher, B. R.; Bawendi, M. G. *Phys. Rev. Lett.* **2010**, *104*, 157403.

(14) Rosen, S.; Schwartz, O.; Oron, D. *Phys. Rev. Lett.* **2010**, *104*, 157404.

(15) Cordones, A. A.; Bixby, T. J.; Leone, S. R. *Nano Lett.* **2011**, *11*, 3366–3369.

(16) Galland, C.; Ghosh, Y.; Steinbrück, A.; Sykora, M.; Hollingsworth, J. A.; Klimov, V. I.; Htoon, H. *Nature* **2011**, *479*, 203–207.

(17) Chen, Y.; Vela, J.; Htoon, H.; Casson, J. L.; Werder, D. J.; Bussian, D. A.; Klimov, V. I.; Hollingsworth, J. A. *J. Am. Chem. Soc.* **2008**, *130*, 5026–5027.

(18) Zhao, J.; Chen, O.; Strasfeld, D. B.; Bawendi, M. G. *Nano Lett.* **2012**, *12*, 4477–4483.

(19) Park, Y.-S.; Ghosh, Y.; Chen, Y.; Piryatinski, A.; Xu, P.; Mack, N. H.; Wang, H.-L.; Klimov, V. I.; Hollingsworth, J. A.; Htoon, H. *Phys. Rev. Lett.* **2013**, *110*, 117401.

(20) Hollingsworth, J. A. *Chem. Mater.* **2013**, *25*, 1318–1331.

(21) Cragg, G. E.; Efros, A. L. *Nano Lett.* **2010**, *10*, 313–317.

(22) García-Santamaría, F.; Brovelli, S.; Viswanatha, R.; Hollingsworth, J. A.; Htoon, H.; Crooker, S. A.; Klimov, V. I. *Nano Lett.* **2011**, *11*, 687–693.

(23) Bae, W. K.; Padilha, L. A.; Park, Y.-S.; McDaniel, H.; Robel, I.; Pietryga, J. M.; Klimov, V. I. *ACS Nano* **2013**, *7*, 3411–3419.

(24) Louyer, Y.; Biadala, L.; Tamarat, P.; Lounis, B. *Appl. Phys. Lett.* **2010**, *96*, 203111.

(25) Fernée, M. J.; Sinito, C.; Louyer, Y.; Potzner, C.; Nguyen, T.-L.; Mulvaney, P.; Tamarat, P.; Lounis, B. *Nat. Commun.* **2012**, *3*, 1287.

(26) Pisanello, F.; Leménager, G.; Martiradonna, L.; Carbone, L.; Vezzoli, S.; Desfonds, P.; Cozzoli, P. D.; Hermier, J.-P.; Giacobino, E.; Cingolani, R.; De Vittorio, M.; Bramati, A. *Adv. Mater.* **2013**, *25*, 1974–1980.

(27) Tenne, R.; Teitelboim, A.; Rukenstein, P.; Dyshel, M.; Mokari, T.; Oron, D. *ACS Nano* **2013**, *7*, 5084–5090.

(28) Talapin, D. V.; Koeppe, R.; Go, S.; Kornowski, A.; Lupton, J. M.; Rogach, A. L.; Benson, O.; Feldmann, J.; Weller, H. *Nano Lett.* **2003**, *3*, 1677–1681.

(29) Carbone, L. et al. *Nano Lett.* **2007**, *7*, 2942–2050.

(30) Talapin, D. V.; Nelson, J. H.; Shevchenko, E. V.; Aloni, S.; Sadtler, B.; Alivisatos, A. P. *Nano Lett.* **2007**, *7*, 2951–2959.

(31) Lupo, M. G.; Della Sala, F.; Carbone, L.; Zavelani-Rossi, M.; Fiore, A.; Lüer, L.; Polli, D.; Cingolani, R.; Manna, L.; Lanzani, G. *Nano Lett.* **2008**, *8*, 4582–4587.

(32) Sitt, A.; Della Sala, F.; Menagen, G.; Banin, U. *Nano Lett.* **2009**, *9*, 3470–3476.

(33) Saba, M.; Minniberger, S.; Quochi, F.; Roither, J.; Marceddu, M.; Gocalinska, A.; Kovalenko, M. V.; Talapin, D. V.; Heiss, W.; Mura, A.; Bongiovanni, G. *Adv. Mater.* **2009**, *21*, 4942–4946.

(34) Zavelani-Rossi, M.; Lupo, M. G.; Tassone, F.; Manna, L.; Lanzani, G. *Nano Lett.* **2010**, *10*, 3142–3150.

(35) She, C.; Demortière, A.; Shevchenko, E. V.; Pelton, M. *J. Phys. Chem. Lett.* **2011**, *2*, 1469–1475.

(36) Kunneman, L. T.; Zanella, M.; Manna, L.; Siebbeles, L. D. A.; Schins, J. M. *J. Phys. Chem. C* **2013**, *117*, 3146–3151.

(37) Jha, P. P.; Guyot-Sionnest, P. *ACS Nano* **2009**, *3*, 1011–1015.

(38) Bajzer, Z.; Therneau, T. M.; Sharp, J. C.; Prendergast, F. G. *Eur. Biophys. J.* **1991**, *20*, 247–262.

(39) Nair, G.; Zhao, J.; Bawendi, M. G. *Nano Lett.* **2011**, *11*, 1136–1140.

(40) Zhang, K.; Chang, H.; Fu, A.; Alivisatos, A. P.; Yang, H. *Nano Lett.* **2006**, *6*, 843–847.

(41) Empedocles, S. A.; Norris, D. J.; Bawendi, M. G. *Phys. Rev. Lett.* **1996**, *77*, 3873–3876.

(42) Neuhauser, R. G.; Shimizu, K. T.; Woo, W. K.; Empedocles, S. A.; Bawendi, M. G. *Phys. Rev. Lett.* **2000**, *85*, 3301–3304.

(43) Brokmann, X.; Coolen, L.; Dahan, M.; Hermier, J. *Phys. Rev. Lett.* **2004**, *93*, 107403.

(44) Leistikow, M. D.; Johansen, J.; Kettelarij, A. J.; Lodahl, P.; Vos, W. L. *Phys. Rev. B* **2009**, *79*, 045301.

(45) Kwadrin, A.; Koenderink, A. F. *J. Phys. Chem. C* **2012**, *116*, 16666–16673.

(46) Lunnemann, P.; Rabouw, F. T.; van Dijk-Moes, R. J. A.; Pietra, F.; Vanmaekelbergh, D.; Koenderink, A. F. *ACS Nano* **2013**, *7*, 5984–5992.

(47) Frantsuzov, P. A.; Marcus, R. A. *Phys. Rev. B* **2005**, *72*, 155321.

(48) Frantsuzov, P. A.; Volkán-Kacsó, S.; Jankó, B. *Phys. Rev. Lett.* **2009**, *103*, 207402.

(49) Shabaev, A.; Rodina, A. V.; Efros, A. L. *Phys. Rev. B* **2012**, *86*, 205311.

(50) Müller, J.; Lupton, J. M.; Lagoudakis, P. G.; Schindler, F.; Koeppe, R.; Rogach, A. L.; Feldmann, J.; Talapin, D. V.; Weller, H. *Nano Lett.* **2005**, *5*, 2044–2049.

(51) Steiner, D.; Dorfs, D.; Banin, U.; Sala, F. D.; Manna, L.; Millo, O. *Nano Lett.* **2008**, *8*, 2954–2958.

(52) Luo, Y.; Wang, L.-W. *ACS Nano* **2010**, *4*, 91–98.

(53) Oron, D.; Kazes, M.; Shweky, I.; Banin, U. *Phys. Rev. B* **2006**, *74*, 115333.

(54) Saba, M.; Aresti, M.; Quochi, F.; Marceddu, M.; Loi, M. A.; Huang, J.; Talapin, D. V.; Mura, A.; Bongiovanni, G. *ACS Nano* **2013**, *7*, 229–238.

(55) Kuno, M.; Fromm, D. P.; Hamann, H. F.; Gallagher, A.; Nesbitt, D. J. *J. Chem. Phys.* **2001**, *115*, 1028.

(56) Cordones, A. A.; Bixby, T. J.; Leone, S. R. *J. Phys. Chem. C* **2011**, *115*, 6341–6349.

(57) Peterson, J. J.; Nesbitt, D. J. *Nano Lett.* **2009**, *9*, 338–345.

(58) Morello, G.; Della Sala, F.; Carbone, L.; Manna, L.; Maruccio, G.; Cingolani, R.; De Giorgi, M. *Phys. Rev. B* **2008**, *78*, 195313.

(59) Smith, A. M.; Mohs, A. M.; Nie, S. *Nature Nanotech.* **2009**, *4*, 56–63.

(60) Smith, E. R.; Luther, J. M.; Johnson, J. C. *Nano Lett.* **2011**, *11*, 4923–4931.

(61) Hughes, S. M.; Alivisatos, A. P. *Nano Lett.* **2013**, *13*, 106–110.

(62) Bertoni, G.; Grillo, V.; Brescia, R.; Ke, X.; Bals, S.; Catellani, A.; Li, H.; Manna, L. *ACS Nano* **2012**, *6*, 6453–6461.

(63) Climente, J. I.; Movilla, J. L.; Planelles, J. *Small* **2012**, *8*, 754–759.

(64) Dennis, A. M.; Mangum, B. D.; Piryatinski, A.; Park, Y.-S.; Hannah, D. C.; Casson, J. L.; Williams, D. J.; Schaller, R. D.; Htoon, H.; Hollingsworth, J. A. *Nano Lett.* **2012**, *12*, 5545–51.

(65) Kharchenko, V. A.; Rosen, M. *J. Lumin.* **1996**, *70*, 158–169.

(66) Klimov, V. I.; Mikhailovsky, A. A.; McBranch, D. W.; Leatherdale, C. A.; Bawendi, M. G. *Science* **2000**, *287*, 1011–1013.

(67) De Mello Donegá, C. *Chem. Soc. Rev.* **2011**, *40*, 1512–1546.

(68) Koole, R.; Van Schooneveld, M. M.; Hilhorst, J.; Donegá, C. D. M.; Hart, D. C.; Van Blaaderen, A.; Vanmaekelbergh, D.; Meijerink, A. *Chem. Mater.* **2008**, *20*, 2503–2512.

(69) Kobayashi, Y.; Misawa, K.; Kobayashi, M.; Takeda, M.; Konno, M.; Satake, M.; Kawazoe, Y.; Ohuchi, N.; Kasuya, A. *Colloids Surf. A* **2004**, *242*, 47–52.

(70) Frimmer, M.; Chen, Y.; Koenderink, A. F. *Phys. Rev. Lett.* **2011**, *107*, 123602.

(71) Leatherdale, C. A.; Woo, W.-K.; Mikulec, F. V.; Bawendi, M. G. *J. Phys. Chem. B* **2002**, *106*, 7619–7622.

For TOC only

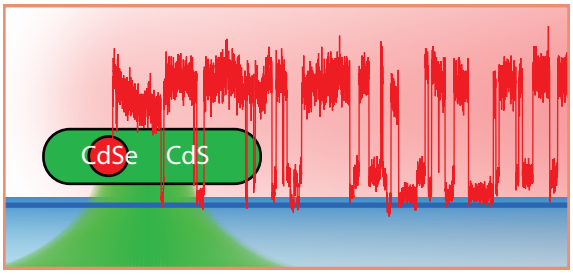

Supplementary Information to Reduced Auger recombination in single CdSe/CdS nanorods by one-dimensional electron delocalization

Freddy T. Rabouw,[1] Per Lunnemann,[2] Relinde J. A. van Dijk-Moes,[1] Martin Frimmer,[2] Francesca Pietra,[1] A. Femius Koenderink,[2] and Daniël Vanmaekelbergh[1]

[1]*Condensed Matter and Interfaces, Debye Institute for Nanomaterials Science, Princetonplein 1, 3584 CC Utrecht, The Netherlands*
[2]*Center for Nanophotonics, FOM Institute for Atomic and Molecular Physics (AMOLF), Science Park 102, 1098 XG Amsterdam, The Netherlands*

TABLE OF CONTENTS

I. FITS TO THE STATE-AVERAGED PL DECAY CURVES AND EMISSION SPECTRA

We used single exponential decay functions to fit the state-resolved PL decay curves (Fig. 2a and Figs. S2c–S19c):

$$I(t) = A \exp\left(-t/\tau\right),$$

where the fit parameters A and τ are the PL decay amplitude and PL lifetime, respectively. We used a maximum-likelihood routine for the fits [1], assuming Poissonian statistics. A flat background was not included since the dark count rate of our detectors is < 10 cts/s. For PL decay curves with a longer lifetime tail, we fitted only to the single exponential early-time signal. The values of the PL decay amplitudes A given (Table 1 and summaries in Figs. S2–S19) are corrected for the relatively short laser repetition period ($T = 100$ ns) of our setup compared to the PL lifetimes (τ = 5–50 ns): $A \rightarrow A/[1 + \exp\left(-T/\tau\right)]$. A correction is needed because the tail of a PL decay curve with $t > T$ is counted towards the early-time signal ($t \rightarrow t - T$), as clearly visible in the PL decay curve of state A (Fig. 2a and Figs. S2c–19c): the signal at negative delay is the tail of the PL decay that extends over longer than 100 ns.

State-averaged emission spectra (Fig. 2b and Figs. S2e–S19e) are asymmetrically broadened towards the red side due to exciton-phonon coupling. They were fitted to a series of phonon replicas at fixed energy intervals of $\epsilon_{\mathrm{LO}} = 26$ meV (the longitudinal optical phonon energy in CdSe) using a nonlinear least-squares method:

$$I(E) = I_0 \sum_{n=0}^{5} \frac{S^n}{n!} \exp\left[-\frac{1}{2}\left(\frac{E - E_0 + n\epsilon_{\mathrm{LO}}}{\sigma}\right)^2\right],$$

Here the fit parameters I_0, E_0, σ and S are the peak amplitude, zero-phonon peak energy, peak width and Huang-Rhys factor, respectively. We obtained typical values for the Huang-Rhys factor of S = 0.3–1.2. The choice for a Gaussian lineshape for each phonon replica is set by broadening due to coupling to lower-energy phonon modes. We find typical values for the peak width of σ = 30–40 meV.

II. REMARKS ON THE TWO METHODS FOR ESTIMATION OF RADIATIVE AND NON-RADIATIVE DECAY CONSTANTS

For reliable estimates of radiative and non-radiative contributions the excitation rate of the emitter must be roughly the same for each state. We have chosen our excitation wavelength (532 nm; 2.34 eV) such that this condition is fulfilled to within an estimated $\pm 10\%$. Two effects must be prevented as much as possible. (1) First, there may be differences between the absorption spectra of the charged and the uncharged state of the NR, due to orbital filling and Stark effects. Transient absorption measurements on ensembles of excited CdSe/CdS NRs [2, 3] and CdSe/CdS thick-shell QDs [4] revealed reduced absorption compared to ground-state emitters over a wide range of photon energies, ranging from the band-edge up to the blue. At the excitation wavelength we use, photoinduced absorption changes are relatively small: $\pm 10\%$, as measured for CdSe/CdS NRs similar to ours [2]. (2) Secondly, using non-resonant excitation results in hot carriers that cool to the bottom of the CB (electrons) or the top of the VB (holes) with an efficiency that may be $< 100\%$ and dependent on the presence of extra charges. Indeed, hot carrier trapping and/or ejection has been measured in PbSe QDs [5, 6], and CdSe/CdS QDs [7]. In our experiments we excite sufficiently near the band-edge of CdSe that we expect an exciton cooling efficiency close to unity. Considering the above we conclude that potential variations in the excitation rate of different states cause an estimated uncertainty of 10% in our estimates of radiative and non-radiative decay rates.

The two methods employed to estimate radiative and non-radiative decay contributions would yield the exact same result for a perfectly single-exponential PL decay curve, and in the absence of background noise. In Fig. 3a we see, however, that the radiative lifetimes of state B obtained by method 1 (via the photon count rates; open circles) are generally shorter by 10–20% than those obtained by method 2 (via the PL decay amplitude; closed circles). This discrepancy is due to time bins assigned to state B but in which one or more rapid B $\leftrightarrow$ A switching events happen. Hence, some photon counts originating from state A are assigned to state B. The apparent photon count rate of state B is slightly increased, since $M_{\mathrm{A}} > M_{\mathrm{B}}$. At the same time, as visible in Fig. 2b and Figs. S2c–S19c, a weak long lifetime component ($\tau_{\mathrm{A}} > \tau_{\mathrm{B}}$) with low amplitude ($A_{\mathrm{A}} < A_{\mathrm{B}}$) appears in the PL decay curve of state B, so the apparent PL decay amplitude of state B decreases. As a result, method 1 (via the photon count rate) overestimates the radiative decay rate of state B, whereas method 2 (via the PL decay amplitude) underestimates it.

Figure S1 shows that the trends observed in Figure 3 of the main text are robust to conservative assumptions of $\eta_{\mathrm{A}} = 0.75$ and a 20% lower excitation rate of state B compared to state A, rather than $\eta_{\mathrm{A}} = 1$ and equal excitation rates. Still we obtain a negative trion (state B) quantum efficiency of $23(\pm 9)\%$ and a radiative decay rate faster than for the neutral exciton (state A) by a factor $1.89(\pm 0.26)$.

III. THE EFFECTIVE MASS CALCULATION METHOD

We performed quantum-mechanical effective-mass calculations [17] to obtain estimates for the transition energies and radiative decay rates of the neutral exciton, and positive and negative trions in our NRs. Schrödinger's equation was solved using the finite element routine of COMSOL Multiphysics v4.1. We modelled a NR as a spherical CdSe core of 3.2 nm diameter, embedded in a cylindrical CdS rod of 5.6 nm diameter and 21 nm length with the centre of the core at 5 nm from one end of the rod (Fig. 4a). We calculated five different states of the NR: (A) the 1h-state, (B) the 1e-state, (C) the 1e1h-state (= exciton X^0), (D) the 1e2h-state (= positive trion X^+), and (E) the 2e1h-state (= negative trion X^-).

A. The 1h-state

Because of the strong confinement and large VB offset between CdS and CdSe, we always modelled the hole as a particle-in-a-spherical-box with infinite potential walls:

$$\left[-\frac{\hbar^2}{2m_h^*}\nabla^2 + V_{\mathrm{vb}}(\mathbf{r})\right]\psi_h(\mathbf{r}) = E_h\psi_h(\mathbf{r}),$$

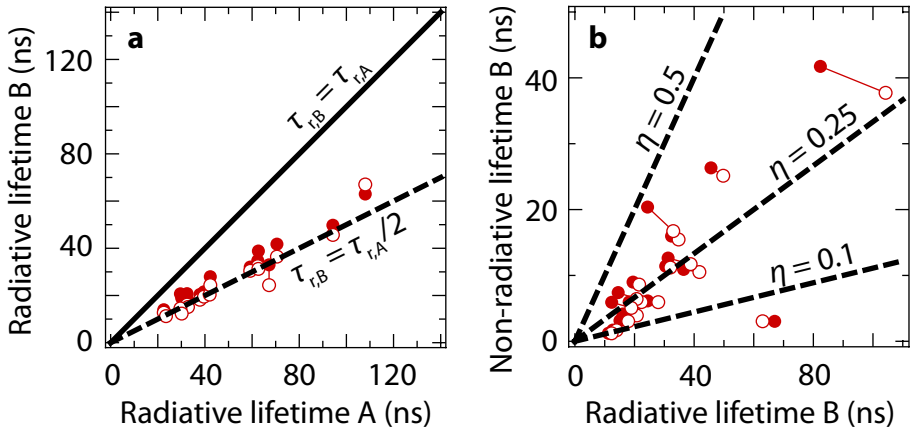

FIG. 1. **Overview of the characteristics of the grey state B for 18 single NRs, under the assumption that $\eta_A = 0.75$ and 20% lower excitation rate of state B compared to state A.** Estimates obtained by method 1 (via the photon count rate; see text for details) are given in open circles, those obtained by method 2 (via the PL decay amplitude; see text for details) in closed disks. Solid lines connect symbols that belong to the same NR, i.e. the results of method 1 and 2. **a)** The correlation between the radiative lifetimes of the bright state A (the neutral exciton X^0) and the grey state B (the negative trion X^-). Radiative decay is faster in the grey state than in the bright state by a factor $1.89(\pm 0.26)$ (mean $\pm$ standard deviation). **b)** The correlation between the radiative and non-radiative lifetimes of the grey state. The resulting quantum efficiency of the grey state is $23(\pm 9)\%$.

where we took $m_h^* = 0.45 m_0$ [18] for the hole effective mass in CdSe, and approximated the top of the VB as an infinite potential well

$$V_{\text{vb}}(\mathbf{r}) = \begin{cases} 0 & ; \ \mathbf{r} \in \text{CdSe} \\ \infty & ; \ \mathbf{r} \in \text{elsewhere} \end{cases}$$

The ground state ψ_h and corresponding energy E_h are directly the solutions for the 1h-state of the NR. In a next step we calculated the Coulomb potential $\phi_h(\mathbf{r})$ due to the hole ground state ψ_h by solving Poisson's equation

$$\nabla^2 \phi_h(\mathbf{r}) = \frac{e\,|\psi_h(\mathbf{r})|^2}{\epsilon \epsilon_0},$$

where we took a dielectric constant of $\epsilon = 10$ in all space. To ensure that ϕ_h approach zero at infinity, we imposed a boundary condition on a spherical surface far from the nanorod:

$$\phi_h(|\mathbf{r} - \mathbf{r}_0| = 250 \text{ nm}) = \frac{e}{4\pi\epsilon\epsilon_0} \times \frac{1}{250 \text{ nm}} = 0.576 \text{ mV},$$

with $\mathbf{r}_0$ the center of the CdSe core.

B. The 1e-state

The electron wavefunctions and energies for the 1e-state are calculated by solving

$$\left[\frac{-\hbar^2}{2m_e^*(\mathbf{r})}\nabla^2 + V_{\text{cb}}(\mathbf{r})\right]\psi_e(\mathbf{r}) = E_e \psi_e(\mathbf{r}),$$

where the electron effective mass [18]

$$m_e^*(\mathbf{r}) = \begin{cases} 0.13 m_0 & ; \ \mathbf{r} \in \text{CdSe} \\ 0.21 m_0 & ; \ \mathbf{r} \in \text{elsewhere} \end{cases}$$

and the bottom of the conduction band

$$V_{\text{cb}}(\mathbf{r}) = \begin{cases} -V_{\text{cbo}} & ; \ \mathbf{r} \in \text{CdSe} \\ 0 & ; \ \mathbf{r} \in \text{CdS} \\ \infty & ; \ \mathbf{r} \in \text{elsewhere} \end{cases}$$

Here we assumed an infinite potential outside the rod. The CB offset between CdSe and CdS is not well known. Different values between $0\ \mathrm{meV}$ and $300\ \mathrm{meV}$ are given in literature [8–10]. Therefore, we performed our calculations for a range of values for the CB offset of $V_{\mathrm{cbo}} = \{0, 50, 100, 200, 300\}\ \mathrm{meV}$.

C. The 1e1h-state (= neutral exciton X^0)

The exciton (1e1h) wavefunction is written as

$$\Psi_{X^0}(\mathbf{r}_e, \mathbf{r}_h) = \psi_{e,X^0}(\mathbf{r}_e)\psi_h(\mathbf{r}_h).$$

Here we assume that the hole part ψ_h is equal to the wavefunction of the 1h-state, since the shape is determined by strong confinement. On the other hand, we allow the electron part ψ_{e,X^0} to adjust (compared to the 1e-state ψ_e) under the influence of Coulomb attraction from the hole. We solve

$$\left[\frac{-\hbar^2}{2m_e^*(\mathbf{r})}\nabla^2 + V_{\mathrm{cb}}(\mathbf{r}) - e\phi_h(\mathbf{r})\right]\psi_{e,X^0}(\mathbf{r}) = E_{e,X^0}\psi_{e,X^0}(\mathbf{r})$$

The total energy of the exciton is then given by

$$E_{X^0} = E_{e,X^0} + E_h$$

D. The 1e2h-state (= positive trion X^+)

The positive trion (1e2h) ground state is written as

$$\Psi_{X^+}(\mathbf{r}_e, \mathbf{r}_{h1}, \mathbf{r}_{h2}) = \frac{1}{\sqrt{2}}\psi_{e,X^+}(\mathbf{r}_e)\left[\psi_h(\mathbf{r}_{h1})\overline{\psi_h}(\mathbf{r}_{h2}) - \overline{\psi_h}(\mathbf{r}_{h1})\psi_h(\mathbf{r}_{h2})\right],$$

where ψ_h and $\overline{\psi_h}$ denote two different hole spin projections. Again, we assume the hole part ψ_h equal to the wavefunction of the 1h-state, and allow the electron part ψ_{e,X^+} to adjust under the influence of Coulomb attraction from the two holes. We solve

$$\left[\frac{-\hbar^2}{2m_e^*(\mathbf{r})}\nabla^2 + V_{\mathrm{cb}}(\mathbf{r}) - 2e\phi_h(\mathbf{r})\right]\psi_{e,X^+}(\mathbf{r}) = E_{e,X^+}\psi_{e,X^+}(\mathbf{r})$$

The total energy of the positive trion is then given by

$$E_{X^+} = E_{e,X^+} + 2E_h + J_{hh},$$

where

$$J_{hh} = \int \psi_h(\mathbf{r})e\phi_h(\mathbf{r})\psi_h(\mathbf{r})\,\mathrm{d}^3\mathbf{r}$$

is the hole-hole Coulomb repulsion energy. The value for $J_{hh} = 160.682\ \mathrm{meV}$ obtained from the COMSOL calculations lies within 0.05% of the value of the analytical Coulomb integral $J_{hh} = \int |\psi(\mathbf{r})|^2 \frac{e^2}{4\pi\epsilon\epsilon_0|\mathbf{r}-\mathbf{r}'|}|\psi(\mathbf{r}')|^2\ \mathrm{d}^3\mathbf{r}\,\mathrm{d}^3\mathbf{r}'$ evaluated in Wolfram Mathematica using the analytical particle-in-a- spherical-box ground state for the hole wavefunction $\psi(\mathbf{r})$.

E. The 2e1h-state (= negative trion X^-)

The negative trion (2e1h) ground state (with paired electron spins) is written as

$$\Psi_{X^-}(\mathbf{r}_{e1}, \mathbf{r}_{e2}, \mathbf{r}_h) = \frac{1}{\sqrt{2}}\left[\psi_{e,X^-}(\mathbf{r}_{e1})\overline{\psi_{e,X^-}}(\mathbf{r}_{e2}) - \overline{\psi_{e,X^-}}(\mathbf{r}_{e1})\psi_{e,X^-}(\mathbf{r}_{e2})\right]\psi_h(\mathbf{r}_h)$$

Again, we assume the hole part ψ_h equal to the wavefunction of the 1h-state, and allow the wavefunction ψ_{e,X^-} of the two electrons to adjust under the influence of Coulomb attraction from the hole and mutual Coulomb repulsion. We solve for ψ_{e,X^-}

using an iterative procedure. We use the electron wavefunction ψ^i_{e,X^-} from iteration step i to obtain the Coulomb potential $\phi^i_e(\mathbf{r})$ using the Poisson equation:

$$\nabla^2\phi^i_e(\mathbf{r}) = \frac{e\left|\psi^i_e(\mathbf{r})\right|^2}{\epsilon\epsilon_0},$$

with the dielectric constant and the boundary condition as before for ϕ_h. Then we solve the electron wavefunction ψ^{i+1}_{e,X^-} of the next iterative step from the Schrödinger equation

$$\left[\frac{-\hbar^2}{2m^*_e(\mathbf{r})}\nabla^2 + V_{\text{cb}}(\mathbf{r}) - e\phi_h(\mathbf{r}) + e\phi^i_e(\mathbf{r})\right]\psi^{i+1}_{e,X^-}(\mathbf{r}) = E^{i+1}_{e,X^-}\psi^{i+1}_{e,X^-}(\mathbf{r})$$

This procedure is repeated until we obtain a self-consistent electron wavefunction and energy. Typically after less than 10 iterative steps the energy E_{e,X^-} has converged to within $1\ \text{meV}$. For the initial guess of the electron wavefunction we use the electron wavefunction of the neutral exciton state $\psi^1_{e,X^-} = \psi_{e,X^0}$. The energy of the negative trion is given by

$$E_{X^-} = 2E_{e,X^-} + E_h - J_{ee}$$

where the term

$$J_{ee} = \int \psi_{e,X^-}(\mathbf{r})e\phi_{e,X^-}(\mathbf{r})\psi_{e,X^-}(\mathbf{r})\,\mathrm{d}^3\mathbf{r}$$

is subtracted to avoid double counting of the electron-electron repulsion.

F. Radiative transition rates

Radiative transition rates can now be obtained from the electron-hole overlap integrals [11]:

$$\tau^{-1}_{\text{r},X^0} = \frac{1}{2}C\left|\int \psi_{e,X^0}(\mathbf{r})\psi_h(\mathbf{r})\,\mathrm{d}^3\mathbf{r}\right|^2$$
$$\tau^{-1}_{\text{r},X^\pm} = C\left|\int \psi_{e,X^\pm}(\mathbf{r})\psi_h(\mathbf{r})\,\mathrm{d}^3\mathbf{r}\right|^2$$

The factor $\frac{1}{2}$ in the expression for τ^{-1}_{r,X^0} accounts for the fact that only one spin-projection of the electron allows recombination with the hole (or equivalently, there is 50% thermal population of dark exciton states [11, 12]). The prefactor $C = \frac{4e^2\omega n P^2|\chi|^2}{9\times 4\pi\epsilon_0 m_0^2 c^3\hbar} = 1/(8.7\ \text{ns})$, where n is the refractive index of the environment ($n = 1.5$ for glass), P is the Kane interband matrix element ($2P^2/m_0 = 19.0\ \text{eV}$ for CdSe [11]), and χ is a local field factor accounting for the local density of optical states on the position of the NR. We take $\chi = \frac{3n^2}{2n^2+n^2_{\text{CdSe}}} = 0.685$, ignoring the asymmetric shape of the NR, and the presence of air above the sample. The approximate value for χ only affects the absolute values obtained for the radiative decay rates, and do not lead to different ratios of the rates of X^0, X^- and X^+.

G. Transition energies

The transition energies of X^0, X^- and X^+ can now be determined from the energies of the states calculated above, and the band gap energy. In the calculations we took the bottom of the CB in CdS as $E = 0$ for the electrons, and the top of the VB in CdSe as $E = 0$ for the holes. Then the transition energies are given by

$$\Delta E_{X^0} = E_{X^0} + E_g + V_{\text{cbo}}$$
$$\Delta E_{X^+} = E_{X^+} - E_h + E_g + V_{\text{cbo}}$$
$$\Delta E_{X^-} = E_{X^-} - \left[\sum_i E^i_e\left|\int \psi_{e,X^-}(\mathbf{r})\psi^i_e(\mathbf{r})\,\mathrm{d}^3\mathbf{r}\right|^2\right] + E_g + V_{\text{cbo}}$$

where the summation over 1e-states ψ^i_e accounts for a finite probability for radiative decay of the negative trion to excited single-electron states (compare Ref. 13), and $E_g = 1.7\ \text{eV}$ is the band gap energy of CdSe. The single-electron energy states are

closely spaced in energy (typical separation $25\ \mathrm{meV}$), so that separate lines are not distinguished in the emission spectra which are already broadened by phonon coupling.

The absolute values for transition energy that we calculate, are some 200 meV higher than those obtained experimentally. The discrepancy can be attributed to the uncertainty in the exact positions of CB and VB extremes, and an overestimation of the hole confinement energy (due to the approximation of infinite potential outside the CdSe core). Fortunately, however, these parameters do not affect the differences in transition energy of X^0, X^- and X^+ that we required in the main text for our assignment of the sign of the trion charge.

IV. DISCUSSION OF THE TRANSITION ENERGIES

The differences in transition energy simulated for the X^0, X^-, and X^+ states (Fig. 4b) can already be understood qualitatively in terms of electron delocalization. To this end we write the transition energies as

$$\begin{aligned}\Delta E_{X^0} &= E^{(0)} - J_{eh}\\ \Delta E_{X^-} &= E^{(0)} - 2J_{eh} + J_{ee}\\ \Delta E_{X^+} &= E^{(0)} - 2J_{eh} + J_{hh}\end{aligned}$$

where $E^{(0)}$ is the zeroth-order transition energy not including electron-hole interactions, i.e. only containing the band gap energy and electron and hole confinement energies. The terms J_{ij} denote the absolute value of the Coulomb interaction energy between carriers i and j. The value of a Coulomb term J_{ij} scales with the average of the inverse distance between carriers i and j. Since the electron wavefunctions are more extended than the hole wavefunctions, $J_{ee} < J_{eh} < J_{hh}$, i.e. electron-electron repulsion is weaker than electron-hole attraction which in turn is weaker than hole-hole repulsion. Therefore we find in Fig. 4b that in order of increasing transition energy $\Delta E_{X^-} < \Delta E_{X^0} < \Delta E_{X^+}$.

Previous spectral studies of single CdSe/CdS nanocrystals at room temperature [19–21] have not presented any indication for emission wavelength blinking as we observe it (Fig. 1c). The difference with our observation presumably stems from the long integration times used previously (1–3 s/frame) and a very low trion quantum efficiency. Montiel and Yang [22] have reported a correlation between emission intensity and wavelength for single CdSe/ZnS QDs, however not from direct spectral measurements but using a pair of band-pass filters and point detectors. On the other hand, there are clear reports of emission wavelength blinking of single CdSe/ZnS nanocrystals at helium temperatures [23, 24], ascribed to exciton-trion switching. In these studies only spectral (no PL decay) measurements were performed, with time resolutions of $100\ \mathrm{ms}$ [23] and $1\ \mathrm{s}$ [24]. The separation between the narrow emission lines for the exciton and the trion is 10–22 meV in Ref. 23 and $< 10\ \mathrm{meV}$ in Ref. 24, in line with our results obtained at room temperature and at a higher time resolution.

V. QUENCHING OF BIEXCITON EMISSION

From photon-photon correlation $g^{(2)}$ plots (Fig. 1a inset, and Figs. S2a–S19a) one can determine the quantum efficiency of the biexciton state X_2. Nair *et al.* [28] have shown that, in the limit of low excitation rates, the height of the zero-delay peak in a normalized $g^{(2)}$ plot is equal to ratio of X_2 quantum efficiency to X^0 quantum efficiency. For our NRs a zero-delay peak cannot be distinguished, hence X_2 emission is completely quenched. Clearly, the biexciton can still effectively decay via a non-radiative (Auger) pathway although we have seen that for the negative trion Auger decay is suppressed. The difference in Auger recombination rates of trion and biexciton has been observed and discussed before for the case of thick-shell CdSe/CdS QDs [15, 29], and is a consequence of the asymmetric confinement of CB electrons and valence band (VB) holes. The 'negative trion Auger pathway' in which a remaining electron accepts the recombination energy, is suppressed as evident from the high X^- quantum efficiency in our NRs. Non-radiative decay of X_2, however, can still be very fast via the 'positive trion Auger pathway', in which a remaining hole is the acceptor carrier. Indeed, the positive trion pathway is expected to be efficient in our NRs, since holes experience a hard confinement potential due to a large VB offset.

VI. DISCUSSION OF THE LOWEST-INTENSITY STATE C

All 18 NRs exhibit a clear low-intensity state B similar to the one of the NR discussed in detail in the main text (see Figs. S3–S19 below). The characteristics of the lowest-intensity state C are much less uniform. 4 out of 18 NRs studied (NRs #1, 2, 7, 18) do not show a state C at all. Those that do can roughly be divided in two groups. For 5 out of 18 NRs (#4, 5, 6, 10, 17) state C has a photon count rate approximately 40% lower and a PL lifetime approximately 40% shorter than state B. We tentatively

assign this state to the double-negative NR, in which non-radiative Auger decay from X^{2-} is enhanced compared to X^{-} since there are two potential acceptor electrons for the recombination energy. A state with similar characteristics has been observed in thick-shell CdSe/CdS QDs [14, 15] and assigned to X^{2-}. For 9 out of 18 NRs (#3, 8, 9, 11, 12, 13, 14, 15, 16) state C has a very low intensity of $< 3\%$ of the high-intensity state, and a very short lifetime (1–2 ns). We tentatively assign this state to the positive NR, in which emission from X^{+} is strongly quenched because the non-radiative "positive trion pathway" is so efficient. The high efficiency of the positive trion pathway is evident from the low biexciton quantum efficiency, and is discussed in the Supplementary Information (Section VI). Another possible explanation of these very-low-intensity C states is given by Qin and Guyot-Sionnest, who associate the lowest intensity periods with oxidation reactions on the surface of CdSe/CdS QDs [16].

VII. FIGURES S2–S19: OVERVIEW OF THE RESULTS FOR ALL 18 SINGLE NRS EXAMINED

The results for all 18 single NRs examined are presented on the following pages (Figs. S2–S19). We present an overview of our entire data set here so that the reader can properly judge the similarities and variations between the different individual NRs. Careful inspection of the data will reveal features (e.g. an apparent correlation between the quality of the Poissonian fit to the intensity histogram and the single exponential character of the PL decay curve) that are beyond the scope of this article to fully investigate and discuss. However, we do hope that such features can inspire future research.

Each of the 18 figures is arranged as follows. **a)** The photon-photon correlation plot, proving the observation of a single NR. **b)** The fluorescence-lifetime-intensity-distribution (FLID) and the corresponding intensity histogram. For computational advantages we use the parameter of average lifetime $\langle\tau\rangle = \sum N_i t_i / \sum N_i$ (where N_i is the number of photon counts at delay time t_i) in these FLIDs, rather than fitted lifetime as in the FLID presented in the main text. The dashed white boxes indicate the different states identified. Red lines in the intensity histogram are fits to Poissonian distributions (obtained with a least-squares method). **c)** State-resolved PL decay curves, obtained by averaging data from time bins highlighted in **b**, for state A (green), B (red), and C (blue). Solid black lines are single exponential fits. **d)** The emission-wavelength-intensity-distribution (EWID) and the corresponding intensity histogram. Again, dashed white boxes indicate the different states identified. **e)** State-resolved emission spectra, obtained by averaging data from spectral frames highlighted in **d**, for state A (green), B (red), and C (blue). Solid lines are fits to a series of phonon replicas. The table at the top-right summarizes the photon count rate M, PL decay amplitude A, lifetime τ, and zero-phonon emission peak energy E_0 for the states identified for the NR.

We remark that in many FLIDs the different states are still distinct, but they appear connected by "smearing". This effect has been discussed before by Galland *et al.* [14], and can be ascribed by rapid charging/discharging events that occur on a time-scale faster than a time bin ($10\ \mathrm{ms}$). Time bins in which the NR switches between state A and B, result in weighted average photon count rates and average lifetimes.

[1] Bajzer, Z., Therneau, T. M., Sharp, J. C. & Prendergast, F. G. Maximum likelihood method for the analysis of time-resolved fluorescence decay curves, *Eur. Biophys. J.* **20**, 247-262 (1991)

[2] Lupo, M. G. *et al.* Ultrafast electron-hole dynamics in core/shell CdSe/CdS dot/rod nanocrystals, *Nano Lett.* **8**, 12, 4582-4587 (2008)

[3] Lupo, M. G. *et al.* Band-edge ultrafast pump-probe spectroscopy of core/shell CdSe/CdS rods: assessing electron delocalization by effective max calculations, *Phys. Chem. Chem. Phys.* **14**, 7420-7426 (2012)

[4] Marceddu, M. *et al.* Charged excitons, Auger recombination and optical gain in CdSe/CdS nanocrystals, *Nanotechnology* **23**, 015201 (2012)

[5] Padilha, L. A. *et al.* Spectral dependence of nanocrystal photoionization probability: the role of hot-carrier transfer, *ACS Nano* **5**, 6, 5045-5055 (2011)

[6] Tisdale, W. A. *et al.* Hot-electron transfer from semiconductor nanocrystals, *Science* **328**, 1543 (2010)

[7] Li, S., Steigerwald, M. L. & Brus. L. E. Surface states in the photoionization of high-quality CdSe core/shell nanocrystals, *ACS Nano* **3**, 5, 1267-1273 (2009)

[8] Müller, J. *et al.* Wave function engineering in elongated semiconductor nanocrystals with heterogeneous carrier confinement, *Nano Lett.* **5**, 2044-2049 (2005)

[9] Steiner, D. *et al.* Determination of band offsets in heterostructured colloidal nanorods using scanning tunneling spectroscopy, *Nano Lett.* **8**, 2954-2958 (2008)

[10] Luo, Y. & Wang, L.-W. Electronic structures of the CdSe/CdS core-shell nanorods, *ACS Nano* **4**, 1, 91-98 (2010)

[11] Shabaev, A., Rodina, A. V. & Efros, Al. L. Fine structure of the band edge excitons and trions in CdSe/CdS core/shell nanocrystals, *Phys. Rev. B* **86**, 205311 (2012)

[12] Efros, Al. L. *et al.* Band-edge exciton in quantum dots of semiconductors with a degenerate valence band: dark and bright exciton states, *Phys. Rev. B* **54**, 7, 4843-4853 (1996)

[13] Wang, X. *et al.* Non-blinking semiconductor nanocrystals, *Nature* **459**, 686-689 (2009)

[14] Galland, C. *et al.* Two types of luminescence blinking revealed by spectroelectrochemistry of single quantum dots, *Nature* **479**, 203-207 (2011)

[15] Galland, C. *et al.* Lifetime blinking in nonblinking nanocrystal quantum dots, *Nat. Commun.* **3**, 908 (2012)

[16] Qin, W. & Guyot-Sionnest, P. Evidence for the role of holes in blinking: negative and oxidized CdSe/CdS dots, *ACS Nano* **6**, 10, 9125-9132 (2012)

[17] Delerue, C. & Lannoo, M., *NanostructuresTheory and Modelling* (Springer-Verlag, Berlin, 2004)

[18] Brovelli, S. *et al.* Nano-engineered electronhole exchange interaction controls exciton dynamics in coreshell semiconductor nanocrystals, *Nano. Commun.* **2**, 280 (2011)

[19] Müller, J. *et al.* Monitoring surface charge movement in single elongated semiconductor nanocrystals, *Phys. Rev. Lett.* **93**, 16, 167402 (2004)

[20] Müller, J. *et al.* Monitoring surface charge migration in the spectral dynamics of single CdSe/CdS nanodot/nanorod heterostructures, *Phys. Rev. B* **72**, 205339 (2005)

[21] Gmez, D. E., Van Embden, J. & Mulvaney, P. Spectral diffusion of single semiconductor nanocrystals: the influence of the dielectric environment, *Appl. Phys. Lett.* **88**, 154106 (2006)

[22] Montiel, D. & Yang, H. Observation of correlated emission intensity and polarization fluctuations in single CdSe/ZnS quantum dots, *J. Phys. Chem. A* **112**, 9352-9355 (2008)

[23] Shimizu, K. T., Woo, W. K., Fisher, B. R., Eisler, H. J. & Bawendi, M. G. Surface-enhanced emission from single semiconductor nanocrystals, *Phys. Rev. Lett.* **89**, 11, 117401 (2002)

[24] Fernée, M. J., Littleton B. N. & Rubinsztein-Dunlop, H. Detection of bright trion states using the fine structure emission of single CdSe/ZnS colloidal quantum dots, *ACS Nano* **3**, 11, 3762-3768 (2009)

[25] Cragg, G. E. & Efros, Al. L. Suppression of Auger processes in confined structures, *Nano Lett.* **10**, 313-317 (2010)

[26] Climente, J. I., Movilla, J. L. & Planelles, P. Auger recombination suppression in nanocrystals with asymmetric electron-hole confinement, *Small* **8**, 5, 754-759 (2012)

[27] Jha, P. P. & Guyot-Sionnest, P. Trion decay in colloidal quantum dots, *ACS Nano* **3**, 4, 1011-1015 (2009)

[28] Nair, G., Zhao, J. & Bawendi, M. G. Biexciton quantum yield of single semiconductor nanocrystals from photon statistics, *Nano Lett.* **11**, 1136-1140 (2011)

[29] Malko, A. V. *et al.* Pump-intensity- and shell-thickness-dependent evolution of photoluminescence blinking in individual core/shell CdSe/CdS nanocrystals, *Nano Lett.* **11**, 5213-5218 (2011)

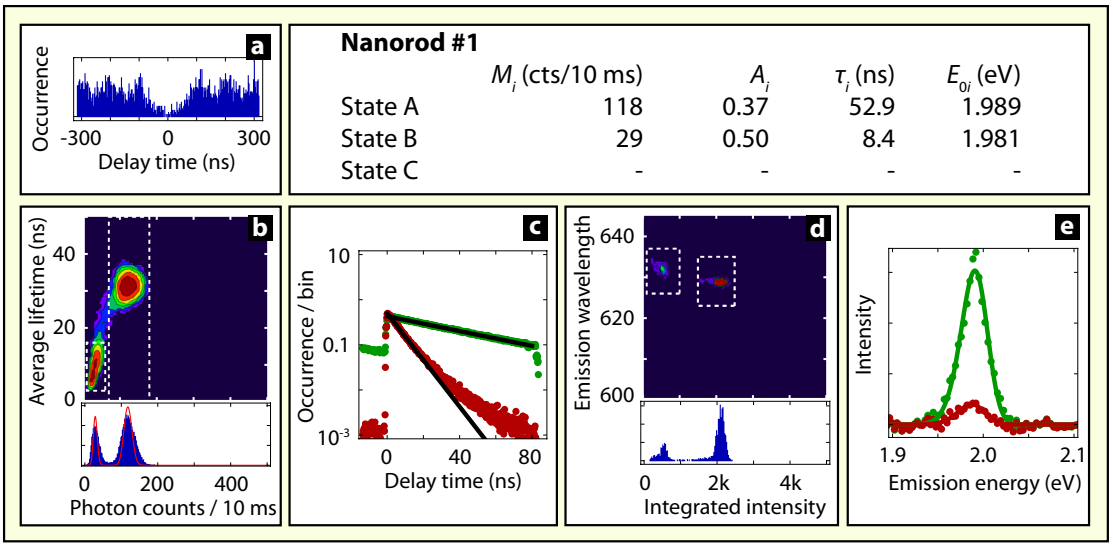

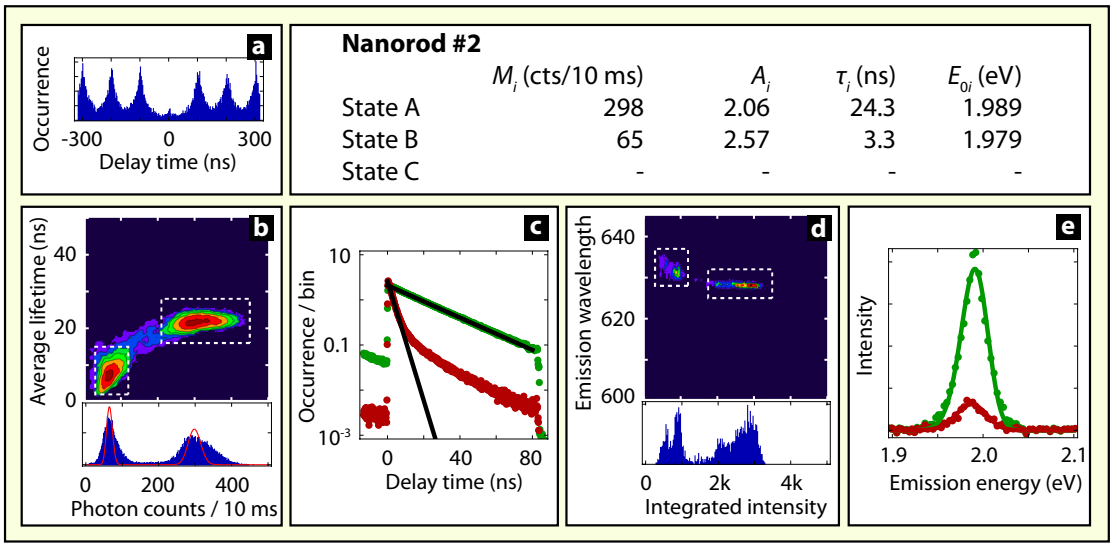

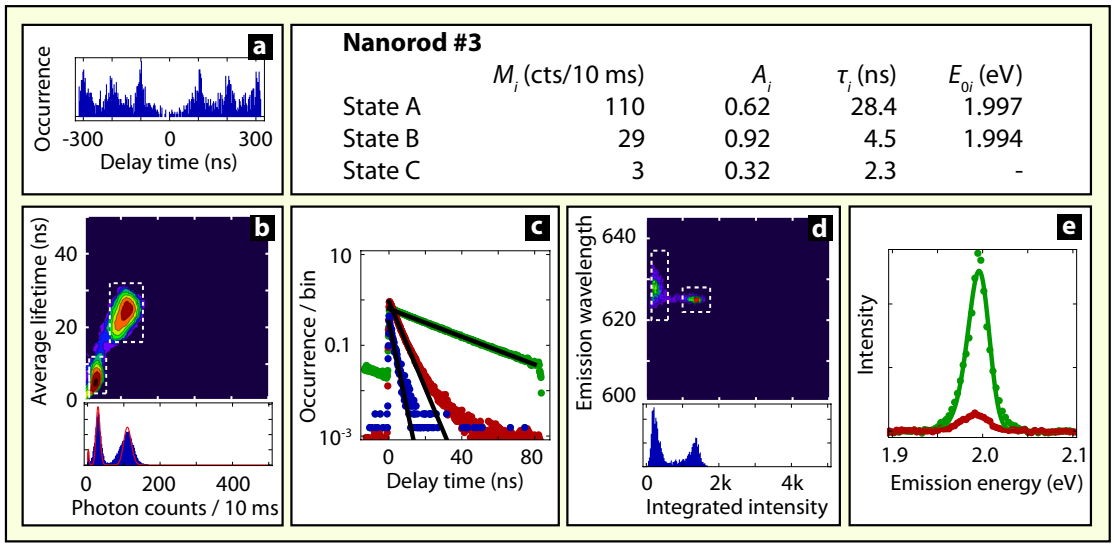

Measurements on nanorods 1, 2, and 3 (see above for description).

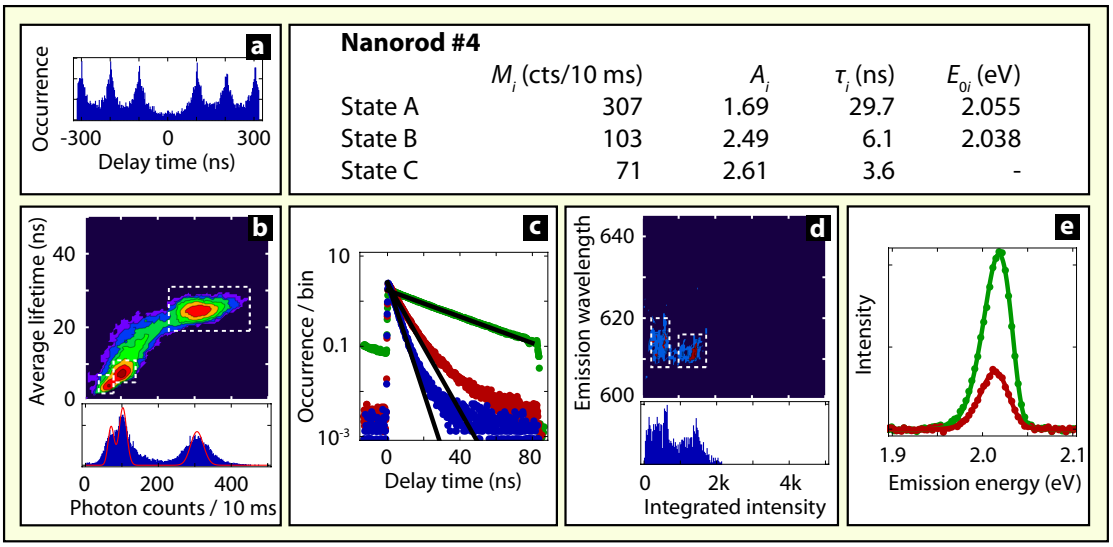

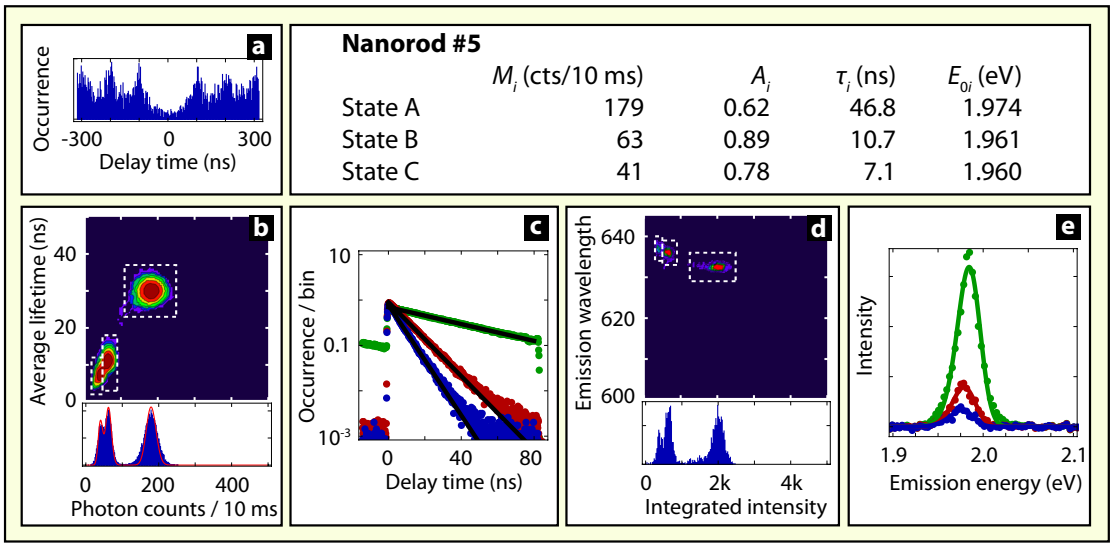

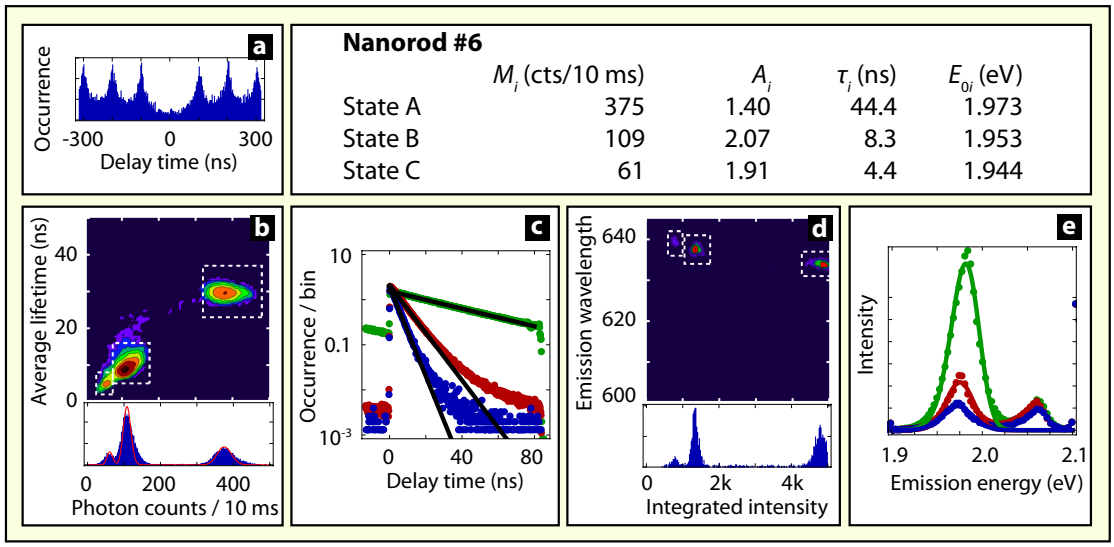

Measurements on nanorods 4, 5, and 6 (see above for description).

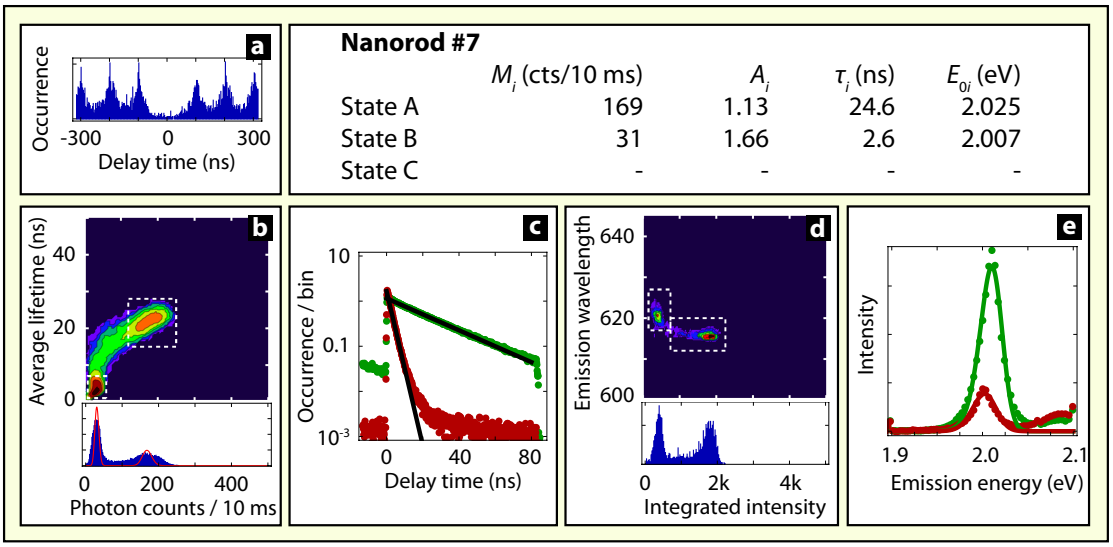

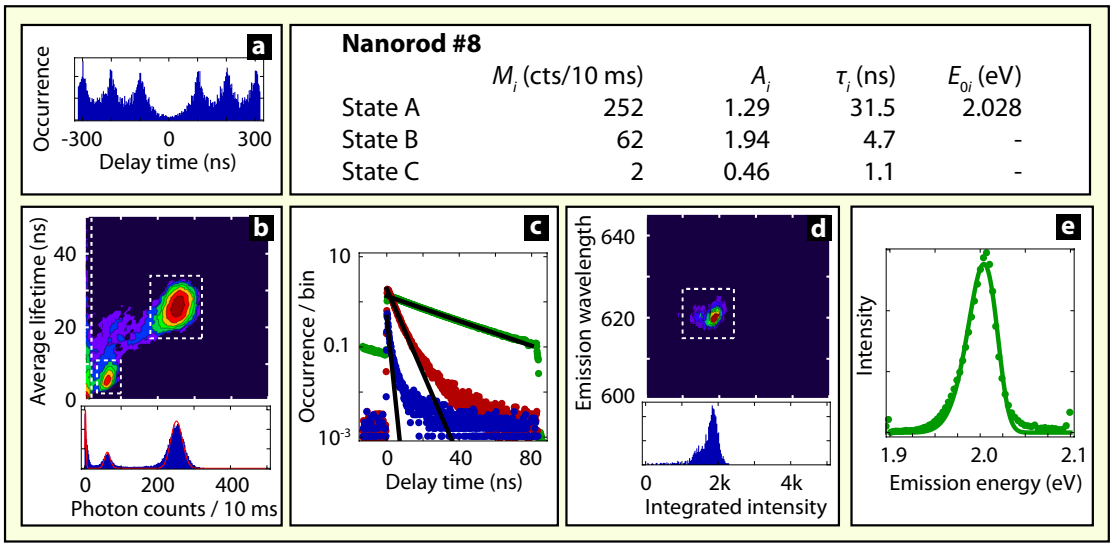

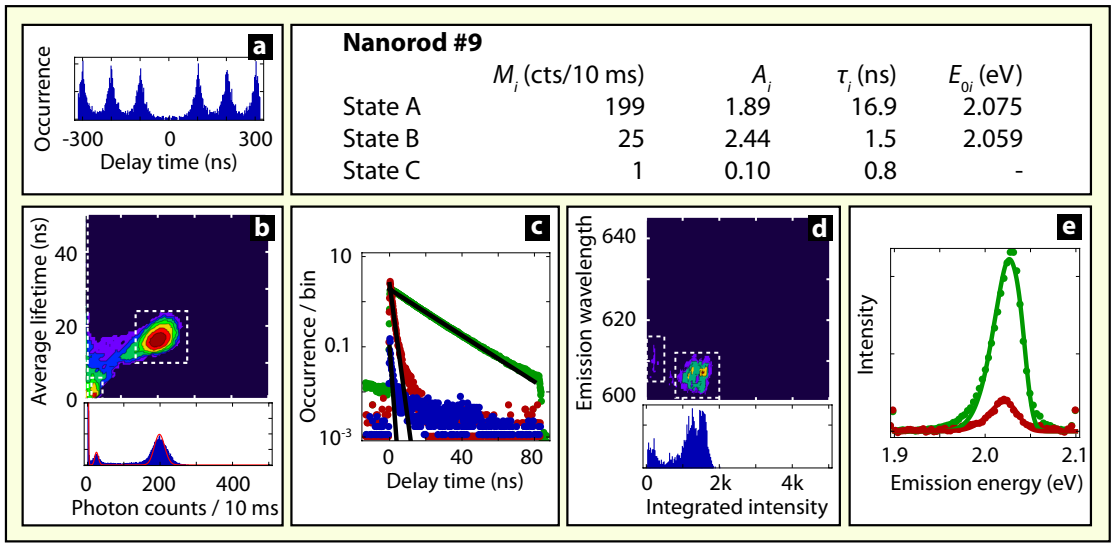

Measurements on nanorods 7, 8, and 9 (see above for description).

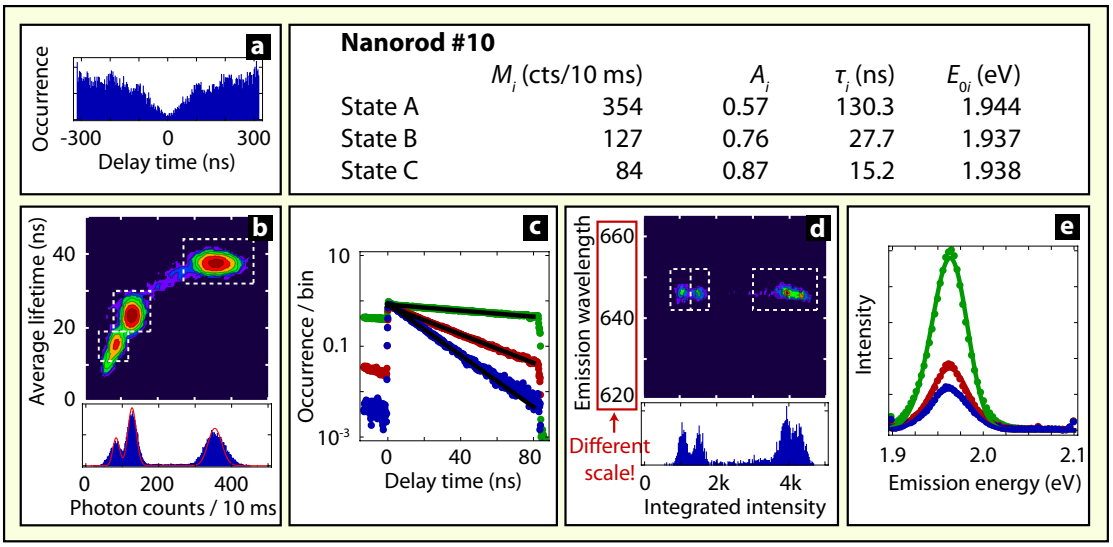

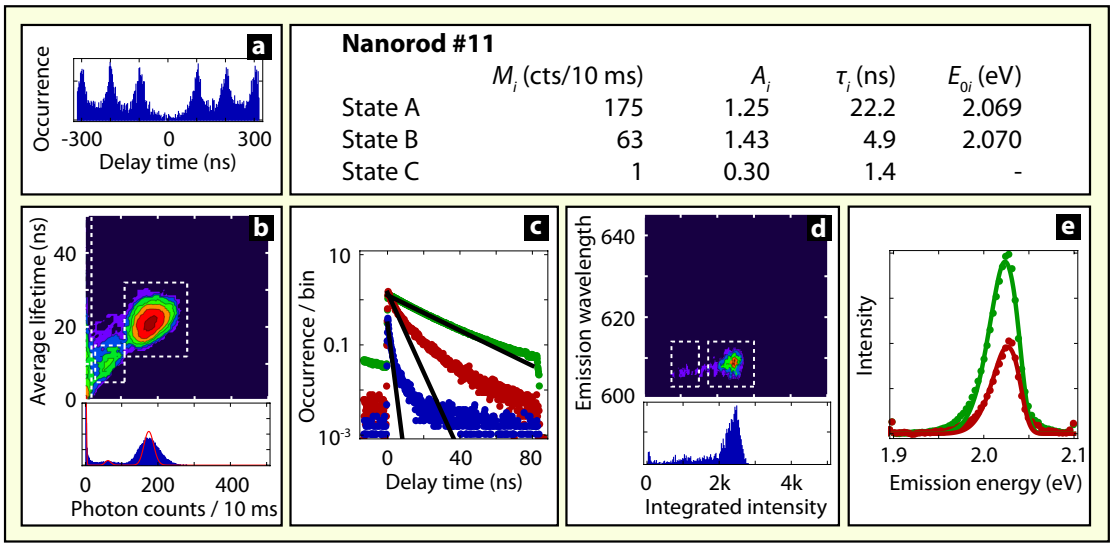

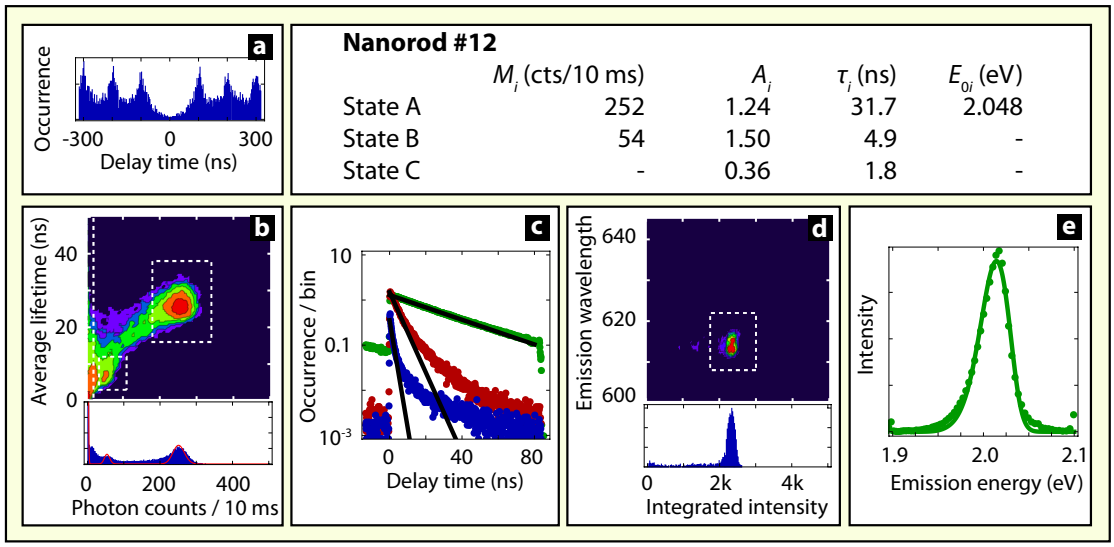

Measurements on nanorods 10, 11, and 12 (see above for description).

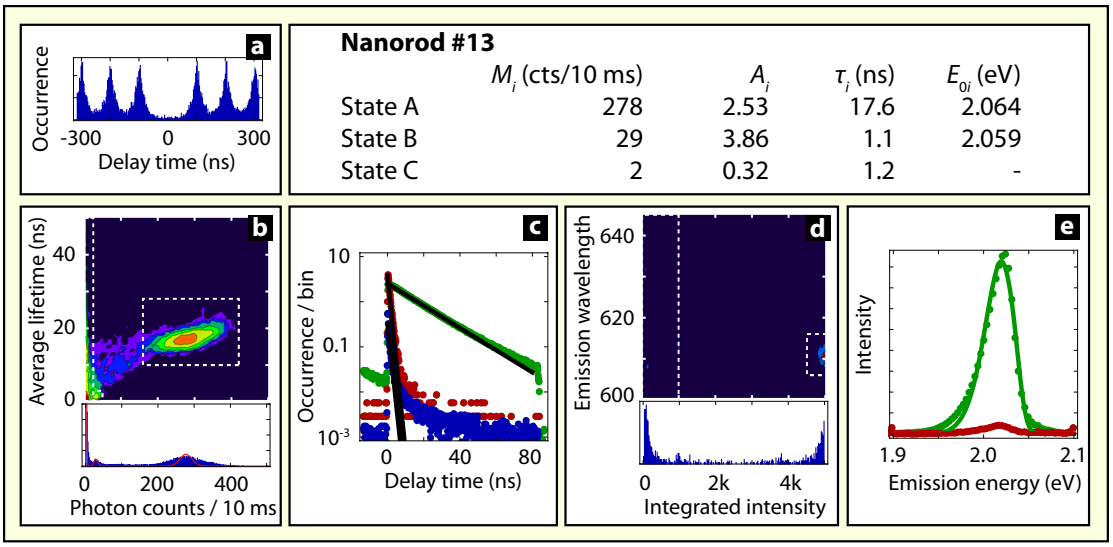

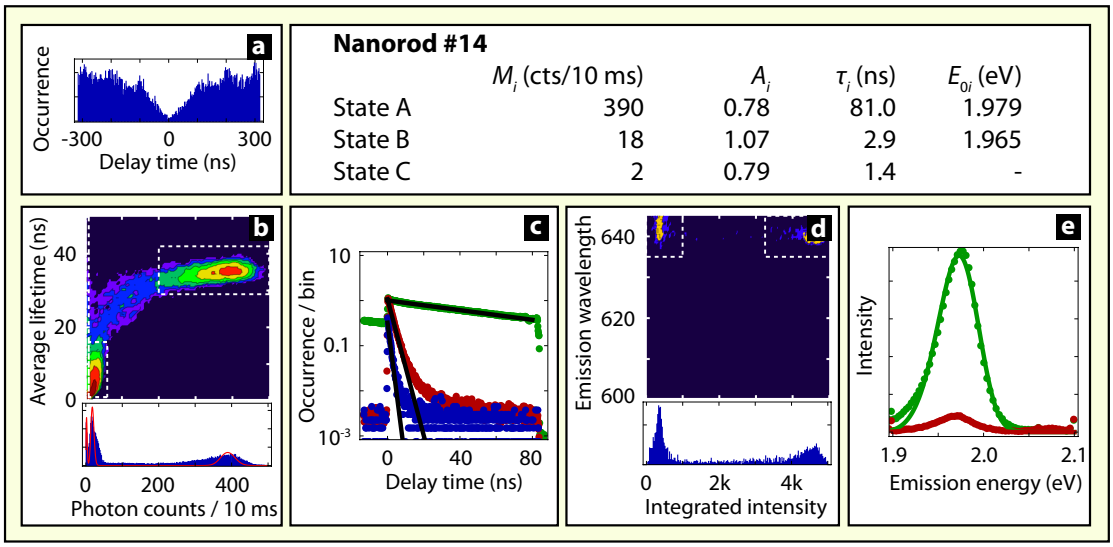

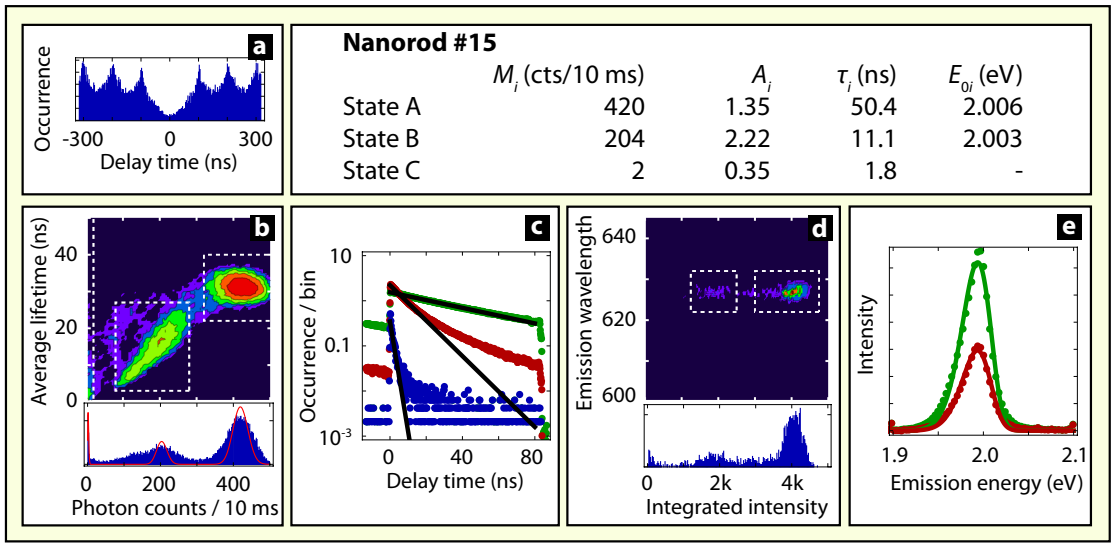

Measurements on nanorods 13, 14, and 15 (see above for description).

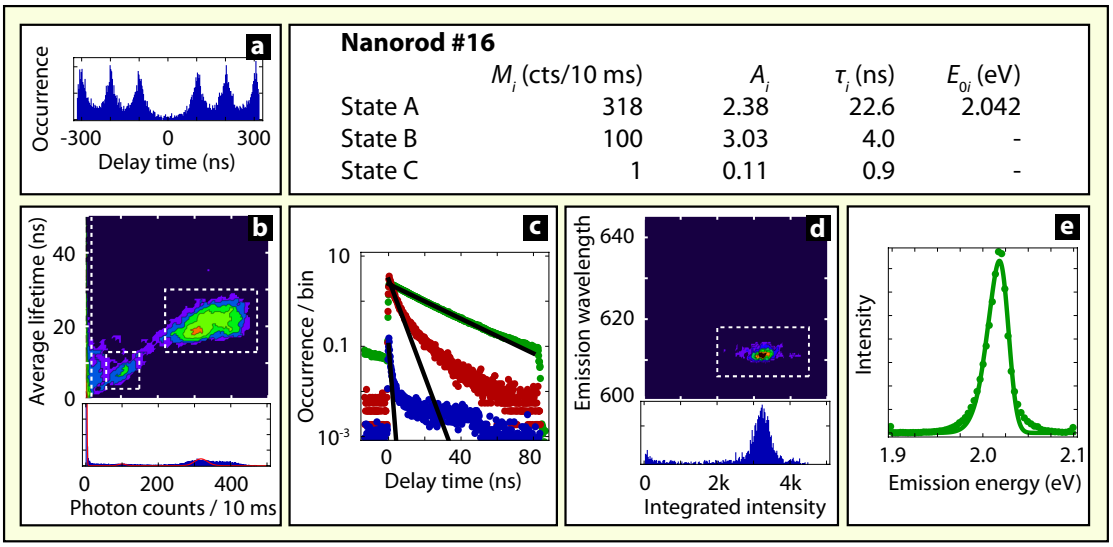

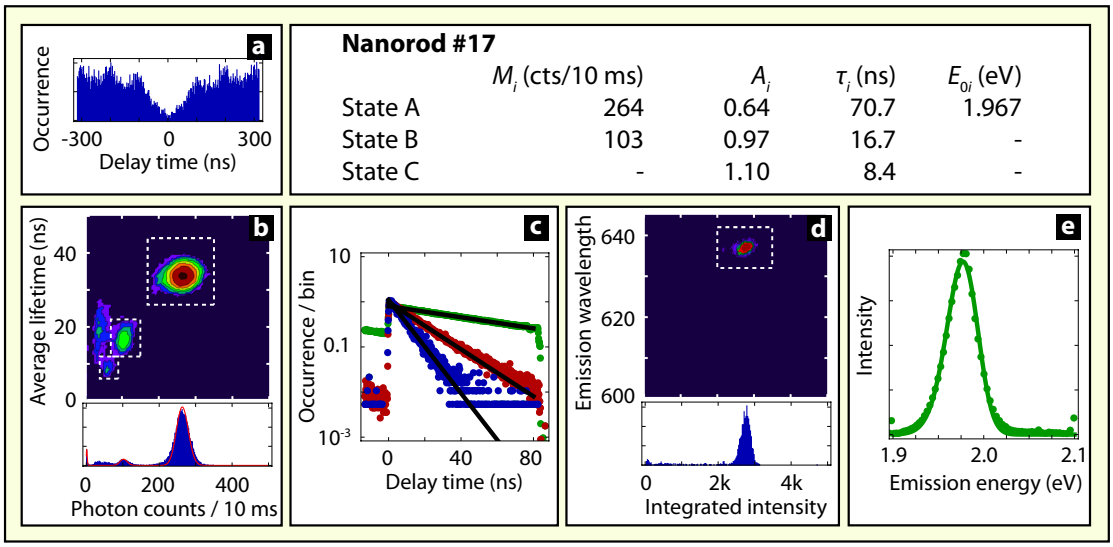

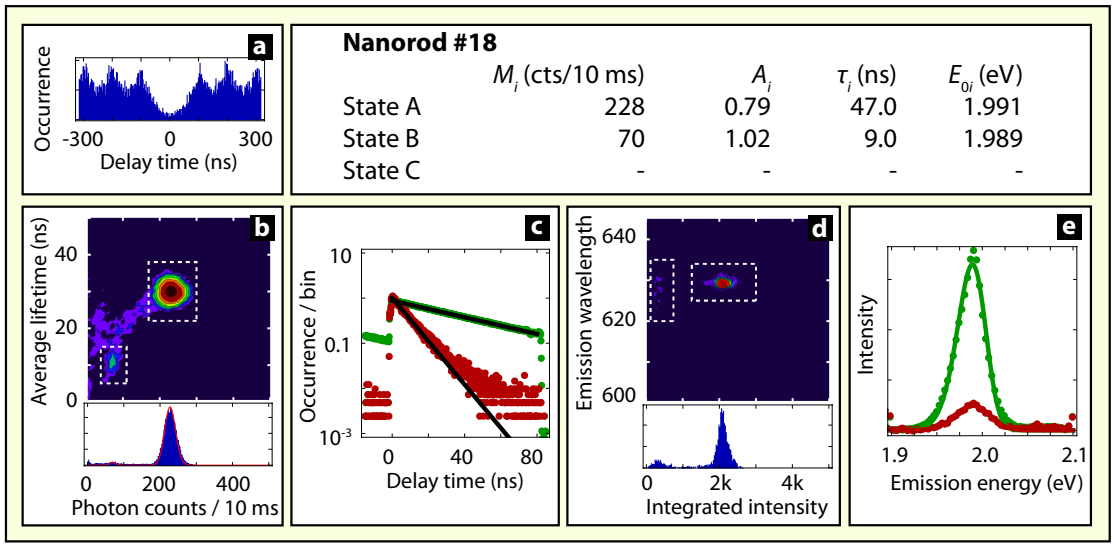

Measurements on nanorods 16, 17, and 18 (see above for description).